Numerical Investigation of Laboratory Tested Cross-Flow Tidal Turbines and Reynolds Number Scaling

R. M. Stringer[a] (corresponding author), A. J. Hillis[b], J. Zang[a]

[a] Department of Architecture and Civil Engineering, University of Bath, Bath, BA2 7AY, UK

[b] Department of Mechanical Engineering, University of Bath, Bath, BA2 7AY, UK

Contact: R. M. Stringer[a]   Tel: +44 (0)1225 386621   Email: r.m.stringer@bath.ac.uk

Abstract

The cross-flow, or vertical axis tidal turbine, is a prominent configuration of marine renewable energy device aimed at converting tidal currents into electrical energy. This paper highlights the hydrodynamic limitations of laboratory testing such devices and uses numerical simulation to explore the effect of device scaling. Using a 2D Reynolds-Averaged Navier-Stokes (RANS) numerical approach, a single turbine blade is initially modelled and validated against published data. The resultant numerical model is then expanded to emulate an experimental cross-flow tidal turbine designed and tested by the University of Oxford. The simulated turbine achieves a close quantitative match for coefficients of power, torque and thrust, forming the basis of a study exploring the effects of Reynolds number scaling in three alternative operating conditions. It is discovered that the coefficient of power (C_P) increases with $\overline{Re}$ without a ubiquitous correlation until an $\overline{Re}$ of ~350,000. Above this $\overline{Re}$ the C_P values for all three operation conditions become both proportional and predictable. The study represents a significant contribution to understanding the application of detailed numerical modelling techniques to cross-flow tidal turbines. The findings, with regard to scaling from laboratory data, could reduce uncertainty and development costs for new and existing devices.

Keywords: Cross-flow; Low Reynolds number; Numerical; RANS; Scaling; Tidal turbine

1. Introduction

The global requirement for clean, economically attractive energy has inspired many innovative tidal energy devices. One such variant, the cross-flow configuration, is explored in this study. This format of device has received growing interest from both academia and industry alike, with leading examples including the University of Oxford 'THAWT' device (now Kepler Energy) [1], and Italian developer Ponti di Archimede Internantional's 'Kobold' turbine [2]. Specifically, the device investigated here is a fixed pitch transverse turbine, designed and experimentally tested by the University of Oxford at laboratory scale. This type of experimental test is typical in the development of any tidal device in order to confirm theoretical and numerical predictions of its proposed hydrodynamic performance. However, downscaling is a complex issue, with reduced turbine performance a common issue due to a number of hydrodynamic effects.

It is well documented that lifting surface performance, namely its lift and drag characteristics, significantly declines at low blade chord Reynolds numbers (Re). In addition, the flow behaviour around many standard foils below a Reynolds number of $\sim 10^5$ becomes rapidly unstable due to a transitional boundary layer. These two factors contribute to the uncertainty of performance scaling particularly in the case of the cross-flow turbine where upstream and downstream blade performance is inherently coupled. Based on this premise, the research presented identifies and explores a number of hydrodynamic limitations of laboratory scale testing of cross-flow tidal turbines. A review of articles on the topic of low Re conditions, both experimental and numerical, is presented and used to inform the numerical strategy of the research.

Using a defined numerical methodology, a mesh sensitivity study is completed for an isolated blade profile in order to assess and maximise the quantitative comparability at lab scale Reynolds numbers. The resulting numerical environment is modified to encompass a 2-dimensional version of the full experimental turbine which is tested at a number of tip speed ratios for validation against experimental data. Finally, the model is used to explore torque, power and thrust outputs for the turbine at increasing diameters up to full scale. Results are plotted against a mean Reynolds number, the intentionally isolated variable, to explore its effects on performance.

1.1 Turbine basics

The concept of the cross-flow device originates from Darrieus' 1931 patent for a wind turbine [3], the theory of which remains applicable to tidal turbines today. Fig. 1 depicts a cross-section of a three bladed cross-flow turbine where the circular line is the blade's flight path around rotational axis z. The direction of rotation is anti-clockwise at angular velocity ω, at radius r, the multiplication of which results in tangential velocity U_t. Components of the oncoming free-stream velocity vector U_∞ and U_t are summed to give local velocity U, as shown in (1), with the average value for one revolution $\overline{U}$ given in (2). Assuming zero losses at the downstream side of the turbine (omitting wake and induction factor losses), α can be calculated using (3), where θ is the azimuth position of the blade as shown in Fig. 1. A key relationship in turbine design, linking free-stream and rotation velocities, is the tip speed ratio (TSR) or λ, as calculated by (4). This relationship is shown in Fig. 2, where α is plotted with increasing θ for λ values of 2, 3 and 4. Operation of the turbine results from the vector sum of the lift L and drag D supplying positive torque to the rotating system.

$$U = \sqrt{(U_\infty \sin\theta)^2 + (U_\infty \cos\theta + U_t)^2} = \frac{U_\infty \sin\theta}{\sin\alpha} \tag{1}$$

where U_∞ is a function of depth (h)

$$\overline{U} = \frac{1}{2\pi}\int_0^{2\pi} U \, d\theta \tag{2}$$

$$\alpha = \tan^{-1}\frac{U_\infty \sin\theta}{U_\infty \cos\theta + U_t} \equiv \tan^{-1}\frac{\sin\theta}{\cos\theta + \lambda} \tag{3}$$

$$TSR = \lambda = \frac{U_t}{U_\infty} \tag{4}$$

$$Re = \frac{\rho U c}{\mu} \tag{5}$$

$$\overline{Re} = \frac{\rho \overline{U} c}{\mu} \tag{6}$$

Evaluating Fig. 2, it is shown that as λ is increased, peak α is decreased and vice versa. The result is that a turbine blade experiences a fluctuating velocity U as a function of the boundary condition U_∞, operating condition λ, and instantaneous position θ. Local velocity U determines the blade chord Reynolds number Re, as calculated by (5); where ρ is fluid density, μ is dynamic viscosity and c is blade chord length. Re is a non-dimensional value representing the relative contributions of inertial and viscous forces acting on the blade, the result of which determines its lift and drag curves, as discussed in section 2. With both absolute and relative values of lift and drag being the primary factors in total turbine performance, Reynolds number provides a suitable factor against which tidal turbines can be characterised, with Froude number (Fr) becoming increasingly important for high blockage, near-surface or surface piecing devices [4]. With both Reynolds and Froude numbers being impossible to satisfy simultaneously over large changes in scale [5], Reynolds number has been chosen for investigation in the current study.

As Re is an instantaneous value, a mean value for one revolution of the turbine, $\overline{Re}$, is used in this research as the independent variable against which turbine performance is equated. The calculation of $\overline{Re}$, given in (6), is not corrected for streamwise induction losses due to the uncertainty of its application for high level resolution models as used in this research. For example, an induction factor loss applied uniformly across the rotor does not account for varying performance of the blades throughout the upstream rotation and hence would not result in reliable velocity corrections for the downstream positions. Additionally, an attempt to establish a value for U_∞ for any given downstream location would require a specified position upstream of the blade to be identified. With the flow velocity subject to high gradients both spatially and temporally, selection of a position too close to the blade and the velocity may already be affected by its wake. Conversely, selection of a position too far from the blade and the velocity is likely to be unrepresentative of the actual flow the blade experiences. A robust approach for highly resolved numerical models is needed if a correction is to be of value, an issue which is currently the subject of ongoing research.

1.2 Experiment Summary

The benchmark for the numerical model is a laboratory test of a cross-flow fixed-pitch tidal turbine conducted at Newcastle University in the combined wind, wave and current tank. The experiment, a preliminary stage assessment of a larger research initiative by the University of Oxford named THAWT (Transverse Horizontal Axis Water Turbine), tested a straight bladed transverse turbine over a range of TSRs. An image of the experimental setup is shown in Fig. 3.

Key features of the experimental test include;

- A three-bladed cross-flow rotor
- Aluminium disk end plates
- Belt driven power take-off coupled to a torque sensor and motor/brake
- Load cell located in a blade to directly measure radially acting force
- A NACA 0018 blade profile, circumferentially mapped such that the chord line falls on the arc of rotation of the blade
- Inclusion of a constriction to allow for the belt drive and instrumentation to be isolated from the flow

A summary of the geometric attributes of the experiment are given in Table 1. For full details of the experimental setup, calibration and error bounds, reference should be made to publications by McAdam [6-8]; It should be noted that the publications present testing from the THAWT rotor, however, the testing equipment and method are identical to the straight-bladed variant presented in this paper.

Parameter	Symbol	Unit	Value
Flume width	b_C	m	1.8
Constriction width	b_T	m	1.61
Flume depth	h	m	1.0
Height of rotor axis above flume base	h_T	m	0.425
Rotor radius	r	m	0.50
Blade length	L_b	m	1.528
Chord length	c	mm	65.45

Table 1. Summary of experimental flume and turbine geometry

Preparation for the experimental test included using an ADCP (Acoustic Doppler Current Profiler) to analyse the current flow at a number of pump power ratings. The profile itself, given in Fig. 4, shows a high level of shear in the flow ranging from 0.363 m/s at the lower boundary of the turbine to 0.275 m/s at the higher, a difference of 25%. Full turbine numerical models of the experiment include an inlet with flow velocities that are interpolated from the original ADV data, further details are given in section 4.1. Turbulence intensity in the experimental flume immediately upstream of the rotor was not available, but was estimated to be ≈1% (from personal correspondence with McAdam [6-8]).

2. Laboratory scale effects

At a nominal TSR of 3, the experimental test has an approximate *Re* range of 35,000 – 80,000, with the lower and higher boundaries representing rotation away from, and towards, the incoming free stream flow respectively. This *Re* range is considered low for an aerofoil, causing a highly transitional boundary layer, laminar separation, and often the formation of a laminar separation bubble [9, 10]. The result is an overall poor performance in terms of lift and drag coefficients; Fig. 5 illustrates this by comparing experimental lift and drag coefficients at three progressively increasing Re for an infinite (or 2D) 0018 NACA profile blade [11, 12]. Examining Fig. 5, lift coefficient is seen to increase with Re, and stall is delayed until higher angles of attack. Similarly, the drag coefficient is higher for low Re cases, decreasing and extending to higher α with increasing Re. A combination of these properties results in a poorer lift to drag ratio. This issue is illustrated by McMasters [13] where an Re value of approximately 10^5 is identified as an average transition point for many aerofoils from a mixed boundary layer (subcritical) to one that is fully turbulent (supercritical). The boundary layer in the subcritical range, where the University of Oxford laboratory test falls, is explored experimentally by Yarusevych [14] at an Re range of 55,000 – 210,000 at 0, 5 and 10 degrees α. Testing with a NACA 0025, two types of boundary layer are observed; at Re values below 135,000 separations without reattachment occur, for values above, the turbulence generated in the shear layer is sufficient to promote reattachment forming a separation bubble. A variant of vortex shedding is also observed throughout the range tested, a phenomenon specific to low Re conditions that is attributed to Kelvin-Helmholts and Tollmien-Schlichting instabilities [15, 16]. Depending on Re, these factors invariably contribute to the reduction in performance previously identified. However, the situation becomes further complicated by the effect of free stream turbulence, an issue experimentally studied by Devinant [17] for aerofoils in Re flows of 100,000 to 700,000. A superior lift and drag performance is observed as turbulence is increased due to delay of boundary separation. This behaviour is achieved numerically using Large Eddy Simulation (LES) by Kim et al. [18]. In a similar manner the surface roughness of the aerofoil can also influence the lift and drag by increasing boundary layer turbulence and thus increasing lift in subcritical flow conditions [13, 19].

Due to the increased flow complexity at low Re, many studies have been conducted to assess and improve the suitability of common numerical methods. The most robust of these is Direct Numerical Simulation (DNS) such as that conducted by Shan et al. [20] and Alam and Sandham [21], however, the mesh densities and timestepping resolution required exclude this method from practical engineering studies [22]. Large Eddy Simulation (LES) is a less computationally expensive method and has been used by Uranga et al. [23] and Catalano & Tognaccin [24], amongst others, to successfully predict pressure and friction distributions as well as vortex instabilities. However, evidence of a superior performance over RANS methods is not explicitly established, particularly for values of lift and drag coefficient, as demonstrated by Yuan [25]. While RANS cannot offer the resolution of the previous methods, the reduced computational effort makes it the most feasible for current engineering activities. A number of publications consider various turbulence models and their suitability to capture both transition and/or lift and drag values. In particular, Windte at al. [26] and Tang [27] both attempt solutions for the SD7003, a low-Re aerofoil, finding the Menter-baseline (BSL) and the Spalart-Allmaras (S-A) models superior respectively. Rumsey and Spalart [28] compare the S-A model with the Shear Stress Transport (SST) models for a NACA 0012 for Re = 100,000. Both models are shown to perform similarly, displaying varying uncertainty with regard to transition onset.

With the SST model proving to be robust at higher Re, as shown by Eleni et al. [29] and Menter [30], adaptions to account for transition have been attempted. A prominent example for general-purpose applications is the SST $\gamma - Re\theta$ transition model developed by Menter et al. [31]. The model adds an intermittency term, γ, and transition momentum thickness Reynolds number, $Re\theta$, to the transport equations of the SST model. The model has been empirically calibrated through experimental comparison and integrated into ANSYS CFX software as described in a paper by Menter et al. [32]. The results of validation studies by Counsil and Boulama [33] and Langtry et al. [31] show that a significant improvement is achieved over the SST in terms surface friction, and to a lesser extent the pressure distribution (due to good baseline performance). Furthermore, the computation of a T106 turbine blade at

$Re \approx 91{,}000$ by Langtry et al. [31] compares steady and unsteady application of the SST $\gamma - Re\theta$ model, finding little variance between the two for pressure distribution.

Predictably, the more computationally intensive numerical methods, such as LES and DNS, provide increased capabilities, particularly the ability to capture the transitional boundary layers and a greater range of turbulent length scale associated with low Re conditions. However, provided that heavy stall is avoided, RANS models can deliver an accurate prediction of lift and drag forces comparable with the higher resolution models. This conclusion led to the selection of a RANS methodology, with test cases being built to compare the SST and SST $\gamma - Re\theta$ turbulence model options. It was found that the $\gamma - Re\theta$ model was particularly sensitive to y^+ and did not converge well close to stall, therefore it was discounted and the standard SST model was chosen as the turbulence model for all further computational modelling.

3. Isolated Blade

The assessment of the individual blade involves the computation of a single aerofoil at angles of attack from 0-25 degrees at a flow speed such that the blade achieves a Reynolds number of 80,000. The study uses symmetrical NACA 0018 blades and a uniform inlet condition to aid validation of the lift and drag components against published data. The resultant numerical and meshing parameters are applied to the cambered blades used in the full turbine model presented in Section 4. In this study the uniform flow testing serves purely as a mesh optimisation exercise, however, research has shown that conformal mapping can be used to predict forces on cambered blades in rotational flow by modelling an equivalent profile in uniform flow [34, 35]. The numerical domain is similar to that used by Wang [36], where a rectangular far-field domain (*Fixed Domain*) with circular sub-domain (*Blade Domain*) is employed, see Fig. 6. The two domains are linked via a sliding mesh that uses a General Grid Interface (GGI) to mathematically resolve the fluxes across the interface [37]. This arrangement allows the *Blade Domain* to pitch the aerofoil without re-meshing and provides a region for high grid refinement.

3.1. Geometry and Boundaries

Dimensionally, the computational domain is sufficiently large to negate blockage errors with the ¼ chord point of the aerofoil (shown in Fig. 6) located at the centroid of both domains. The boundary conditions are as follows:

Inlet – A uniform flow is specified, calculated by rearrangement of the Reynolds number for velocity U, see equation (4). Turbulence at the inlet was set by specifying an intensity I value of 1% (see section 1.2). This is converted into values of turbulence kinetic energy k, turbulence eddy frequency ω and turbulence dissipation ε, in the ANSYS solver using equations (7-10), where μ^t is turbulence viscosity and $C_\mu = 0.09$, a non-dimensional constant.

$$k = \frac{3}{2} {U_\infty}^2 I^2 \tag{7}$$

$$\frac{\mu^t}{\mu} = 1 \tag{8}$$

$$\omega = \rho \frac{k}{\mu^t} \tag{9}$$

$$\varepsilon = C_\mu \rho \frac{k^2}{\mu^t} \tag{10}$$

Outlet – This is set as an 'opening' with a relative static pressure of zero; $P_{rel} = 0$.

Top and bottom – The sides assigned as 'free-slip' boundaries, shown in Fig. 6, allow the fluid velocity component parallel to the wall to remain computed, while velocity normal to the wall and the wall shear stress are set to zero; $U_y = 0, \tau_{wall} = 0$.

Periodic faces – All boundaries in the x-y plane are set as symmetry planes; where normal velocities and advection gradients are set to zero.

Blade surfaces – These surfaces are set to 'no-slip', where pressure is set to zero gradient and velocities are set to zero; $U_x = U_y = 0$.

3.2. Meshing

Alongside the turbulence model selection, meshing strategy is a key means of extracting the best possible outcome from the numerical model. The *Fixed Domain* contains a structured hexahedral mesh that only deforms at the interface with the *Blade Domain.* The interface was divided into 360 cells at both sides allowing for 1:1 cell alignment when the *Blade Domain* is positioned at 1 degree increments. The *Blade Domain*, shown in Fig. 7, is a mixed mesh consisting of a body fitted hexahedral mesh at the blade surface, with the remaining domain filled with wedges. Convergence studies were performed on mesh expansion ratio of the wedges (beyond the body fitted region) and the number of streamwise cells on the blade surface. The result was a low sensitivity to expansion ratio provided that the boundary layer meshing is sufficient, and that streamwise cells below the recommended aspect ratio of 100/1 (width to height) showed little sensitivity provided the ratio wasn't exceeded. The final values of 200 streamwise cells for the upper and lower blade surface, and a wedge expansion ratio of 1.1, were used. This leaves the boundary layer meshing itself as the focus of the testing. In order to capture the desired accuracy of the flow at the boundary layer, as discussed in the background, the meshing is tested for maximum y^+ (or yPlus) values between 1 and 30, see equation (11), where τ_ω is shear stress, y_1 is first layer height, and ν is kinematic viscosity.

$$y^+ = \frac{\sqrt{\frac{\tau_\omega}{\rho}} \times y_1}{\nu} \tag{11}$$

3.3. Solver control

All models were solved using ANSYS CFX 14.0 software (under an academic license), a general purpose Navier-Stokes code. Using a steady state RANS method with a k-ω SST turbulence model, the solutions were completed to a residual target of 10^{-5} for mass and momentum terms.

3.4. Results & Discussion

Coefficients of lift C_L and drag C_D, given in equations (12-13), generated by the numerical models are compared in Fig. 8 alongside the result of an XFOIL V6.99 panel code simulation developed by Drela [38] and experimental data extracted from Jacobs and Sherman [11]. To correspond with the experimental turbine and numerical tests, the XFOIL solutions were computed with a free stream turbulence intensity of 1% (Ncrit = 2.6224). The experimental values from Jacobs and Sherman are corrected by the authors to profile values (infinite aspect ratio), with turbulence estimated to be around 0.5% - 1% for the wind tunnel used [39].

$$C_L = \frac{L}{\frac{1}{2}\rho U^2 c} \tag{12}$$

$$C_D = \frac{D}{\frac{1}{2}\rho U^2 c} \tag{13}$$

The experimental C_L values are closely matched by all computed y^+ (written yPlus on Fig 8.) solutions up to the onset of stall at an α of 11°, with a maximum error of ≈5%. The stall point is delayed by the numerical models by +1° to 2° similar to the XFOIL result. Post-stall the SST model predicts a fluctuating lift force, as would be experienced experimentally, with flat line convergence being unachievable. These fluctuations differ with y^+ with the lowest and highest values, 1 and 30 respectively, displaying the most extreme forces. In terms of drag coefficient, the correlation is very similar, with pre-stall displaying high accuracy and stall being shifted up the same margin as the lift coefficient. Considering the effect of y^+ on the results more closely, divergence is seen as α increases for all pre-stall angles of attack. Additionally, as y^+ increases, C_L is increasingly over-predicted near to stall while conversely, C_D is progressively under-predicted. At a $y^+$of 30 the solution is beginning to diverge from the experimental values with the logarithmic wall model taking a greater part in estimating the near wall flow. In the post-stall region the highly unstable result at a y^+ of 1 is due to the model attempting to resolve the viscous sublayer in full, leading to greater pressure fluctuations at the surface of the blade. Conversely, the highest y^+ is excessively coarse, causing large turbulent structures to form and an unrealistically large C_L to be predicted. Mid-range y^+ values offer high accuracy when predicting C_L and C_D at low α and a more stable solution in post-stall conditions, therefore a y^+ of 10 was chosen for all full turbine model simulations.

While the study gave guidance in terms of maximising the accuracy of forces at achievable angles of attack, it is expected that this range would be extended in the final model due to the effects of dynamic stall. The phenomenon is reported by Wang [36], who finds that the SST model is able to capture the delayed stall of an aerofoil in similar low Re conditions to the current study. In addition, the SST model is known to improve in accuracy with increasing Re, this was confirmed by additional numerical models built to the same constraints as those presented here.

4. Full Turbine Model

A fully transient turbine model was developed and initially solved for TSRs between 2 and 5 for comparison with the Universirty of Oxford straight bladed turbine experimental values. To investigate scale, further solutions are generated at a TSR of 3 for turbines up to a 10 metre diameter. In order to test the robustness of possible scaling trends, additional solutions are run for a TSR of 4, and for a uniform velocity profile.. Table 2 details the numerical tests conducted, where the velocity profile is split into experimental (Exp.) or uniform flows, and $\overline{U_C}$ and $\overline{U_R}$ are mean velocities for the full channel depth and across the rotor respectively (see Fig. 4.)

Test ID	Velocity Profile	$\overline{U_C}$ (m/s)	$\overline{U_R}$ (m/s)	λ	D (m)	$\overline{Re}$
1				2		45,250
2				2.5		55,333
3				3		65,605
4				3.5	0.5	75,984
5				4		86,428
6				4.5		96,915
7				5		107,433
8	Exp.		0.3698		1	131,210
9				3	2.5	328,026
10					5	656,052
11		0.333			10	1,312,104
12					1	172,856
13				4	2.5	432,139
14					5	864,277
15					10	1,728,555
16					0.5	59,112
17					1	118,224
18	Uniform		0.333	3	2.5	295,560
19					5	591,120
20					10	1,182,241

Table 2. Full turbine numerical modelling test scheme

Using a similar multi-domain approach to the isolated blade tests, the model consists of 3 blade domains, a rotating domain, and an outer fixed domain, as shown in Fig. 9. The geometry represents a centre section through the xy plane of the experiment (see Fig. 6), with turbine dimensions being identical and numerical flume height being equal to water depth.

4.1. Numerical Setup

The numerical setup is based on the environment developed in the isolated blade testing in terms of boundaries, governing equations, solver convergence and meshing, with grid sizes ranging from 150,000 to 300,000 nodes. However, the simulation is now transient (unsteady RANS) with solutions running until a quasi-steady result was observed, i.e. varying with equal magnitude with each revolution. The result was considered to be converged when the average torque for 1 revolution deviated from the previous revolution by <1%, this took between 5 and 6 revolutions. Due to the implicit solution method of the software, stable convergence can be achieved at large timestep values. Therefore, timestep size was defined as the period of 0.5° of turbine rotation θ, equating to courant numbers below 100 for all cases.

To convert the 3D experimental case into 2D, a number of assumptions were required. In particular, the effect of the experimental channel constriction is simplified into a velocity increase proportional to the decrease in area of the flume. Figure 10 illustrates this issue, where L_b is turbine blade length, b_T is test width, and b_C is channel width. Assuming water depth change is negligible through the constriction, conservation of momentum dictates that the velocity must increase equal to the ratio of area lost, i.e. b_C/b_T or 1.8/1.61. In the experimental case the rotor region (hashed area on Fig. 10) is aligned centrally within the constriction; note that the narrowing and then widening of the constriction occurs inside of the rotor's upstream and downstream extremities. The position of these constriction changes, and hence velocity, are problematic for the 2D model, therefore it is assumed that the whole turbine is subject to the velocity increase and that TSR is maintained for the upstream half of the rotor, i.e. rotational velocity is calculated from the increased mean inlet velocity. The final inlet of the numerical tank took the form of a depth based interpolation of the original velocity profile (see Fig. 4) multiplied by the area ratio 1.8/1.61. It was confirmed that the numerical model succeeded in propagating the velocity profile from the inlet to the rotor with minimal change.

Having already made the assumption that depth change is negligible, the model also excludes a free surface, instead using a 'free slip' condition at the upper boundary. These simplifications have been previously shown to have little effect on the numerical result for overall turbine torque, see [40].

4.2 Results & Discussion

The experimental data was collected by gradual ramping of the turbine rotation from zero up to a TSR of 5 and back to zero during which torque and force sensors recorded the turbine's responses. Due to the cyclic delivery of the torque, the collected data was smoothed using resampling (see McAdam [6]), from which values of power coefficient C_P, torque C_Q and thrust C_T were calculated. The ramping experimental methodology produced a slight variation in the results between the rising and falling data due to the reaction time of the motor/brake; therefore an average of the two has been taken to produce the final values. A similar mean is calculated for torque Q and thrust T from the numerical result by averaging each value over a single 360° rotation of the turbine, where power $P = Q\lambda$, and thrust is the force equal and opposite to the streamwise drag of the entire rotor. Simulations were computed on the University of Bath 'Aquila' high performance computer taking an average of 48 hours on 4 processors to complete. All values of C_P, C_Q and C_T are based upon the available kinetic energy within the limits of the rotor (see Fig. 4), using equations (14), (15) and (16) respectively, where A is the swept area of the rotor seen by the flow, and U_r is the mean flow velocity within rotor area A.

$$C_P = \frac{P}{\frac{1}{2}\rho A {U_r}^3} \tag{14}$$

$$C_Q = \frac{C_P}{\lambda} \tag{15}$$

$$C_T = \frac{T}{\frac{1}{2}\rho A {U_r}^2} \tag{16}$$

4.2 .1 Lab Scale

All three parameters given in equations (14-16) are plotted in Fig. 11 for experimental and numerical methods. Comparing the two results for C_P shown in Fig. 11 (a), it is clear that the numerical model achieves high correlation with the experiment. At close inspection the numerical result slightly under predicts C_P below a TSR of 3, changing to over prediction by a maximum of ≈10% at a TSR of 4. Qualitatively the numerical result matches the experimental values, showing a rising value of C_P up to a TSR of 4, before losing efficiency and falling as TSR rises to 5. Identical trends for both torque coefficient plotted in Fig. 11 (b), and thrust coefficient in Fig. 11 (c), where the crossing points between numerical and experimental values also fall at a TSR of 3, with peak torque falling at the lower TSR of ~3.6 as would be expected.

The quantitative error of the numerical model can be attributed to a number of limitations. At low TSR the reduced accuracy and marginal under-prediction of forces of the SST model at post-stall angles of attack, as shown in Fig. 8, would explain the lower than expected values. Above a TSR of 3, the over prediction is more significantly influenced by the required simplification of the 3D constriction of the flume into a 2D model. To achieve this the correction requires an increased angular velocity employed in the numerical model to maintain TSR with the corrected inlet velocity, as detailed in section 4.1, and therefore may result in the over prediction of turbine performance.

Despite the limitations imposed by the low Re conditions, the simplified numerical model has accurately predicted trends and quantitative values within a peak error of ±10% for all coefficients. It is worth noting that all numerical results fall into the extremities of the experimental raw data (example shown in McAdam [6]), with the experiment itself being subject to range of instrumentation and experimental error tolerances.

To explore the accuracy of the simulation further, Fig. 12 shows the coefficient of distributed normal load C_N, given in equation (17), for experimental and numerical results for

TSRs of 2, 3 and 4; where N is the distributed normal load. For clarity, the load given is acting radially, where positive values are acting away from the turbine axis (see [7]).

$$C_N = \frac{N}{\frac{1}{2}\rho c U_r^{\,2}} \tag{17}$$

Considering the slowest spinning turbine case, at a TSR of 2, Fig. 12 (a) shows that the numerical simulation achieves broad correlation with experiment, but with diverging force oscillations visible in the 180-360 degree region. Referring to Fig. 1, at rotation angles (θ) below 180 degrees the blades are upstream, and above 180 degrees they are downstream. In the downstream region, due to the low TSR and velocity shadow induced by the upstream wake, the blades experience the lowest blade chord Reynolds numbers modelled in this research, resulting in heavy stall of the downstream blades. In such conditions the unsteady RANS method is unable to accurately resolve the flow shear around the blades resulting in a poor match in this region.

At a TSR of 3, Fig. 12 (b) shows an improved correlation with the experimental readings compared to Fig. 12 (a). The positives include a qualitatively high match, with almost all of the peaks and troughs captured by the numerical model. In particular, the downstream values suggest that the generation and advection of shear flows is taking place with consummate accuracy. The origins of the load force fluctuations are highlighted in Fig. 13 which presents a contour plot of the flow field velocities for the same numerical result. The velocities have been limited to values from 0.125 to 0.625 in order to visually capture the advection of velocity fluctuations generated by the upstream blade wake. By comparing Fig. 12 (b) and Fig. 13 it is possible to correlate the fluctuations in force between θ positions of 170° and 250° to the dynamic vortex shedding shown in the contour plot. Similarly, the wake fluctuations passing the downstream blade between the 270° and 350° positions are also visible in both the force prediction and the contour plot. Quantitatively the zero degree value and the downstream values are below expected. Causes include possible free surface effects for values close to zero degrees and the inability of the 2D model to capture the effect of the diverging flume side walls as shown in Fig. 10.

Increasing the speed of the turbine to a TSR of 4, Fig. 12 (c) shows similar attributes to those in Fig. 12 (b). The upstream quantitative values are particularly well matched with the extreme loading predicted within 5% of the experimental value. Downstream the result diverges more significantly from experimental values and appears as a smoother line.

The reduced forces numerically predicted at the downstream positions for TSRs of 3 and 4 suggest that there is unexpected loss in flow velocity between upstream and downstream locations. Along with the issues raised already in the discussion, this discrepancy may also be a symptom of a higher free stream turbulence than was estimated for the experiment, causing faster wake recovery. Additionally, the influence of the velocity correction to account for the constriction may result in an increased blade efficiency at the upstream position and hence result in a lower flow speed downstream. It should be noted that the experimental plot is an instantaneous result, demonstrated by the 0° and 360° differing in Fig. 12 (a-c), and therefore is subject to variances which may not reflect the exact average of the force acting on the turbine blade.

4.2.2 Turbine Scaling

To explore the effect of Reynolds number scaling on turbine performance a series of simulations were performed at turbine diameters of 0.5m, 1m, 2.5m, 5m and 10m, with 0.5m being the lab scale model. Each test includes a velocity profile equivalent to the lab scale inlet that has stretched depth-wise such that the overall resolved flow velocities and directions experienced by the blade are equal at all scales. The study includes three sets of results (S1, S2 and S3), referring to Table 2, S1 comprises of tests 3, 8-11, S2 from 5, 12-15, and S3 from tests 16-20. The three sets represent three alternative turbine operating conditions, TSR 3 and TSR 4 in the experimental velocity profile, and TSR 3 in uniform flow conditions.

The results for the scaling tests are shown in Fig. 14, where all results are plotted against $\overline{Re}$. Starting with the Coefficient of power in Fig. 14 (a), the three scaling tests are plotted with each marker representing a result at each increment of geometric scaling; the result for test set S1 is labelled as an example. A number of significant findings can be observed, firstly, the power coefficient increases significantly from low $\overline{Re}$, lab scale conditions, up to the full scale equivalent. For example, S1 increases by over 200% from the experimental lab scale, for a rotor experiencing a mean blade chord Reynolds number 20 times higher. Secondly, the rate of increase is non-linear, with all three test cases displaying a decaying increase in C_P. Additionally, the three test cases show little correlation with each other. For example, at low $\overline{Re}$, equivalent to lab scale, S2 gives the highest C_P, S3 medium value, and S1 the lowest. At high $\overline{Re}$ values of $>10^6$, equivalent to a full scale turbine, the order of performance is altered such that S3 provides the highest C_P, S1 medium, and S2 the lowest performing turbine. However, at an $\overline{Re}$ of approximately 350,000 the power coefficients of all three cases rise with equal gradients signifying that the effects of low $\overline{Re}$ conditions are diminishing, with the solution converging towards an asympotote.

Fig. 14 (b) shows the change in torque coefficient with $\overline{Re}$, where C_Q is non-dimensionalised by equation (15). Unlike the plot for C_P the three test results do not cross, but display an otherwise equivalent behaviour.

The final plot, Fig. 14 (c), shows thrust coefficient against $\overline{Re}$. All three sets experience a lower relative thrust at lab scale than would be expected at full scale. In parallel to the C_P, the thrust becomes increasingly constant at an $\overline{Re}$ of ~350,000 and above.

5. Conclusions

An experimental test conducted by the University of Oxford has been used as a basis to develop and validate a numerical model of a three bladed variant of a cross-flow turbine. The resultant model has been adapted to explore performance at increased scales and identify relationships and limitations in both the experimental and numerical methods.

An isolated blade case was used to classify and validate prediction of lift and drag coefficients using a RANS numerical model employing the $k - \omega$ SST turbulence model. The result showed a high degree of correlation with experimental values for all angles of attack below stall, with a maximum error in lift coefficient ≈5%. In post-stall conditions stability of the numerical solution proved to be sensitive to y^+ with values between 10 and 15 found to be the most stable. This range falls directly in the transition region, defined as 11.06 for ω based models, between the linear near wall layer and the logarithmic region of the boundary layer.

The results of the numerical modelling of the University of Oxford laboratory scale turbine confirm that a URANS methodology with 2D simplification is capable of providing accurate hydrodynamic performance predictions for cross-flow turbines. For all practical turbine operation speeds the maximum quantitative error for C_P was 8%, with positive qualitative agreement achieved for all variables (see Fig. 11). Investigating local forces on the blades showed that the numerical model is capturing not only global averages, but also advecting realistic turbulent structures through the turbine in cases where deep stall is avoided. The most prominent example of this is shown in Fig. 12 (b), supported by Fig. 13, where the numerical results capture the downstream fluctuation of C_N due to the generated upstream wake in parallel with the experiment. Limitations to the numerical accuracy of the lab scale result include the negation of the flume narrows, velocity correction and turbulence assumptions, and very low Re ω equation performance in the boundary layer.

Scaling of the turbine was approached by focussing on the changes to device performance with mean blade chord Reynolds number $\overline{Re}$. Based on the high validation achieved at lab scale, and the known improvement to blade force prediction using ω based models at increased Reynolds numbers, a purely numerical series of tests were conducted. The scaling tests, detailed in Table 2, generated a number of findings including:

- At full scale/high Re the turbine achieves significantly higher power coefficients than an equivalent lab scale model
- The increase in power coefficient with scale is non-linear and varies inconsistently between operating conditions for values of $\overline{Re}$ below ~350,000.
- Above an $\overline{Re}$ of ~350,000, the power coefficients of all operating conditions become equally proportional.

The rise in C_P at higher Reynolds numbers is expected and supports existing literature. However, the inconsistency of the increase in C_P between the three operating conditions shown in Fig. 14 shows conclusively that tests both numerically or experimentally do not scale consistently when referenced against mean Reynolds number. For example, Set 2, TSR 4 – experimental flow, was the highest performing of all three cases, but by an $\overline{Re}$ ~250,000 this had fallen to thc worst pcrforming. Thc transition between varying and proportional results falling at ~350,000 is consistent with the boundary layer transformation of the selected foil from a mixed to a supercritical boundary layer, this change is key to the behaviour demonstrated in the results. Additionally, the boundary layer behaviour has the knock-on effect of triggering dynamic stall with leading and trailing edge vortex generation causing turbulent structures that have a non-trivial effect on upstream and downstream blade performance. For these reasons, the results advocate the use of a minimum $\overline{Re}$ of ~350,000 for laboratory scale tests in order to avoid low Re effects and provide scalability and proportionality to the acquired turbine performance data. Furthermore, the reduction in uncertainty may also improve the isolation and application of additional corrections such as accounting for Froude number and blockage. For alternative turbine geometries differing $\overline{Re}$ limits are likely to exist and therefore should be considered alongside other known effects when inferring full scale turbine performance from low Re test data.

6. Acknowledgements

Ross McAdam and Guy Houlsby of the University of Oxford are thanked for providing the experimental data used in this study for validation of the numerical simulations.

References

1. *University of Oxford. Tidal Energy Research Group*. Available from: http://www.eng.ox.ac.uk/tidal/research/thawt.
2. Calcagno, G., et al., *Experimental and numerical investigation of an innovative technology for marine current exploitation: the Kobold turbine.* Proceedings of the Sixteenth (2006) International Offshore and Polar Engineering Conference, Vol 1, 2006: p. 323-330.
3. Darrieus, G.J.M., *Turbine having its rotating shaft transverse to the flow of the current*, U.S.P. Office, Editor. 1931.
4. Lynn, P.A.a., *Electricity from wave and tide : an introduction to marine energy.*
5. Whelan, J. and T. Stallard. *Arguments for modifying the geometry of a scale model rotor.* in *9th European Wave and Tidal Energy Conference (EWTEC2011)*. Southampton.
6. McAdam, R.A., G.T. Houlsby, and M.L.G. Oldfield, *Experimental measurements of the hydrodynamic performance and structural loading of the Transverse Horizontal Axis Water Turbine: Part 1.* Renewable Energy, 2013. **59**(0): p. 105-114.
7. McAdam, R.A., G.T. Houlsby, and M.L.G. Oldfield, *Experimental measurements of the hydrodynamic performance and structural loading of the Transverse Horizontal Axis Water Turbine: Part 2.* Renewable Energy, 2013. **59**: p. 141-149.
8. McAdam, R.A., G.T. Houlsby, and M.L.G. Oldfield, *Experimental measurements of the hydrodynamic performance and structural loading of the Transverse Horizontal Axis Water Turbine: Part 3.* Renewable Energy, 2013. **59**: p. 82-91.
9. Hain, R., C.J. Kahler, and R. Radespiel, *Dynamics of laminar separation bubbles at low-Reynolds-number aerofoils.* Journal of Fluid Mechanics, 2009. **630**: p. 129-153.
10. Selig, M.S., et al., *Experiments on Airfoils at Low Reynolds Numbers.* AIAA Paper 96-0062, 1996.
11. Jacobs, E.N. and A. Sherman, *Airfoil Section Characteristics as Affected by Variations of the Reynolds Number.* NACA Report no. 586, 1937.
12. Jacobs, E.N., K.E. Ward, and R.M. Pinkerton, *The characteristics of 78 related airfoil sections from tests in the variable-density wind tunnel.* NACA Report 460, 1933.
13. Mcmasters, J.H. and M.L. Henderson, *Low-Speed Single Element Airfoil Synthesis.* Technical Soaring, 1979. **4**(2): p. 1-21.
14. Yarusevych, S., P.E. Sullivan, and J.G. Kawall, *On vortex shedding from an airfoil in low-Reynolds-number flows.* Journal of Fluid Mechanics, 2009. **632**: p. 245-271.
15. Lin, J.C.M. and L.L. Pauley, *Low-Reynolds-number separation on an airfoil.* Aiaa Journal, 1996. **34**(8): p. 1570-1577.
16. Brinkerhoff, J.R. and M.I. Yaras, *Interaction of viscous and inviscid instability modes in separation-bubble transition.* Physics of Fluids, 2011. **23**(12).

17. Devinant, P., T. Laverne, and J. Hureau, *Experimental study of wind-turbine airfoil aerodynamics in high turbulence.* Journal of Wind Engineering and Industrial Aerodynamics, 2002. **90**(6): p. 689-707.
18. Kim, Y., Z.T. Xie, and I.P. Castro *LES study of a wind turbine airfoil flow in turbulence.*
19. Santhanakrishnan, A., et al., *Enabling Flow Control Technology for Low Speed UAVs.* 2005.
20. Shan, H., L. Jiang, and C.Q. Liu, *Direct numerical simulation of flow separation around a NACA 0012 airfoil.* Computers & Fluids, 2005. **34**(9): p. 1096-1114.
21. Alam, M. and N.D. Sandham, *Direct numerical simulation of 'short' laminar separation bubbles with turbulent reattachment.* Journal of Fluid Mechanics, 2000. **410**: p. 1-28.
22. Coleman, G.N. and R.D. Sandberg, *A Primer on direct numerical simulation of turbulence - methods, procedures and guidelines.*, in *Tech. Rep AFM-09/01a.* 2010, Aerodynamics & Flight Mechanics Research Group, School of Engineering Sciences. University of Southampton.
23. Uranga Cabrera, A., *Investigation of transition to turbulence at low Reynolds numbers using Implicit Large Eddy Simulations with a Discontinuous Galerkin method.* 2010, Massachusetts Institute of Technology. p. 164 p.
24. Catalano, P. and R. Tognaccini, *Large Eddy Simulations of the Flow around the SD 7003 Airfoil*, in *AIMETA Conference 2011.* 2011: Bologna.
25. Yuan, W., et al., *A parametric study of LES on laminar-turbulent transitional flows past an airfoil.* International Journal of Computational Fluid Dynamics, 2006. **20**(1): p. 45-54.
26. Windte, J., U. Scholz, and R. Radespiel, *Validation of the RANS-simulation of laminar separation bubbles on airfoils.* Aerospace Science and Technology, 2006. **10**(6): p. 484-494.
27. Tang, L., *Reynolds-averaged Navier-Stokes simulation of low-Reynolds-number airfoil aerodynamics.* Journal of Aircraft, 2008. **45**(3): p. 848-856.
28. Rumsey, C.L. and P.R. Spalart, *Turbulence Model Behavior in Low Reynolds Number Regions of Aerodynamic Flowfields.* Aiaa Journal, 2009. **47**(4): p. 982-993.
29. Eleni, D.C., T.I. Athanasios, and M.P. Dionissios, *Evaluation of the turbulence models for the simulation of the flow over a National Advisory Committee for Aeronautics (NACA) 0012 airfoil.*
30. Menter, F.R., *2-Equation Eddy-Viscosity Turbulence Models for Engineering Applications.* Aiaa Journal, 1994. **32**(8): p. 1598-1605.
31. Menter, F.R., R. Langtry, and S. Volker, *Transition modelling for general purpose CFD codes.* Flow Turbulence and Combustion, 2006. **77**(1-4): p. 277-303.
32. Menter, F.R., et al., *A correlation-based transition model using local variables - Part I: Model formulation.* Journal of Turbomachinery-Transactions of the Asme, 2006. **128**(3): p. 413-422.
33. Counsil, J.N.N. and K.G. Boulama, *Validating the URANS shear stress transport gamma - Re-theta model for low-Reynolds-number external aerodynamics.* International Journal for Numerical Methods in Fluids, 2012. **69**(8): p. 1411-1432.

34. Migliore, P.G., W.P. Wolfe, and J.B. Fanucci, *Flow Curvature Effects on Darrieus Turbine Blade Aerodynamics.* Journal of Energy, 1980. **4**(2): p. 49-55.
35. Hiromichi, A., et al., *A conformal mapping technique to correlate the rotating flow around a wing section of vertical axis wind turbine and an equivalent linear flow around a static wing.* Environmental Research Letters, 2013. **8**(4): p. 044040.
36. Wang, S.Y., et al., *Numerical investigations on dynamic stall of low Reynolds number flow around oscillating airfoils.* Computers & Fluids, 2010. **39**(9): p. 1529-1541.
37. Galpin, P.F., R.B. Broberg, and B.R. Hutchinson, *Three-dimensional Navier-Stokes Predictions of Steady State Rotor/Stator Interaction with Pitch Change*, in *Third Annual Conference of CFD Society of Canada*. 1995: Banf, Ontario, Canada.
38. Drela, M., *XFOIL: An analysis and design system for low Reynolds number airfoils*, in *Low Reynolds number aerodynamics*. 1989, Springer. p. 1-12.
39. Dryden, H.L.A., Ira H, *The design of low-turbulence wind tunnels.* National Advisory Committee for Aeronautics, 1948(Technical Note No. 1755).
40. C.A.Consul, R.H.J.W. *An Investigation of the Influence of Free Surface Effects on the Hydrodynamic Performance of Marine Cross-Flow Turbines*. in *9th European Wave and Tidal Energy Conference*. 2011. Southampton, UK.

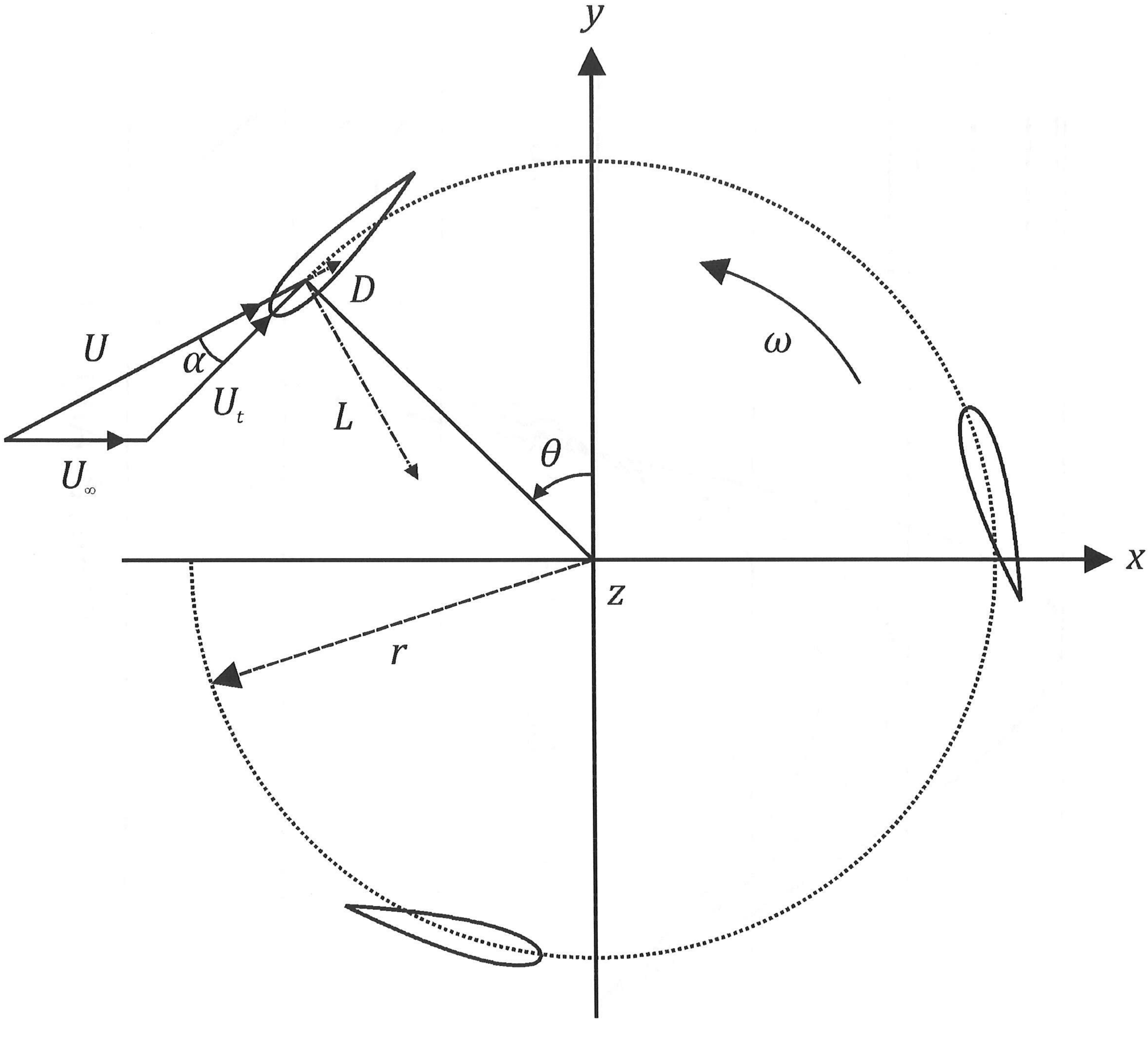
y
x
z
D
U
α
U_t
L
U_∞
θ
ω
r

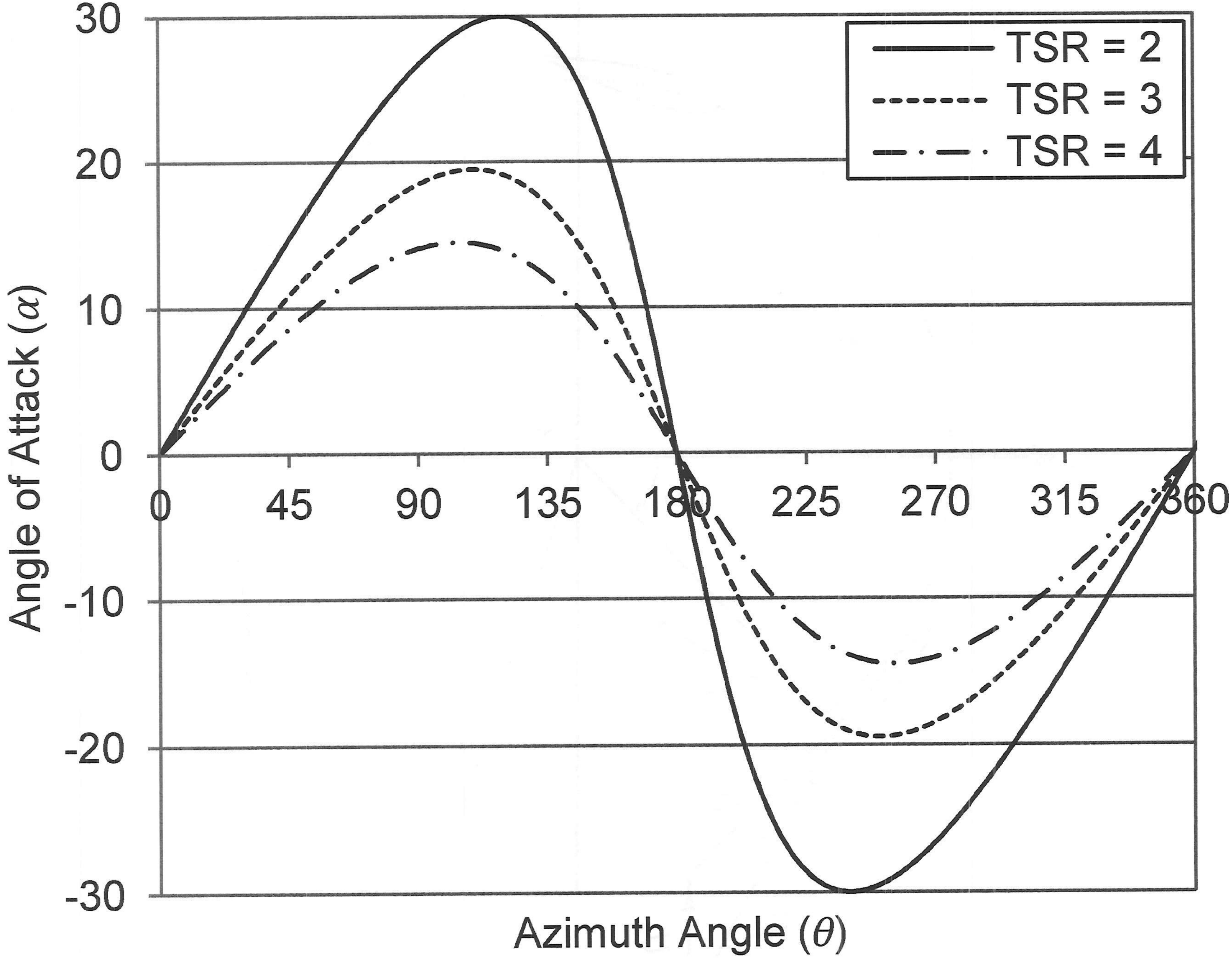

TSR = 2
TSR = 3
TSR = 4
30
20
10
0
-10
-20
-30
0
45
90
135
180
225
270
315
360
Angle of Attack (α)
Azimuth Angle (θ)

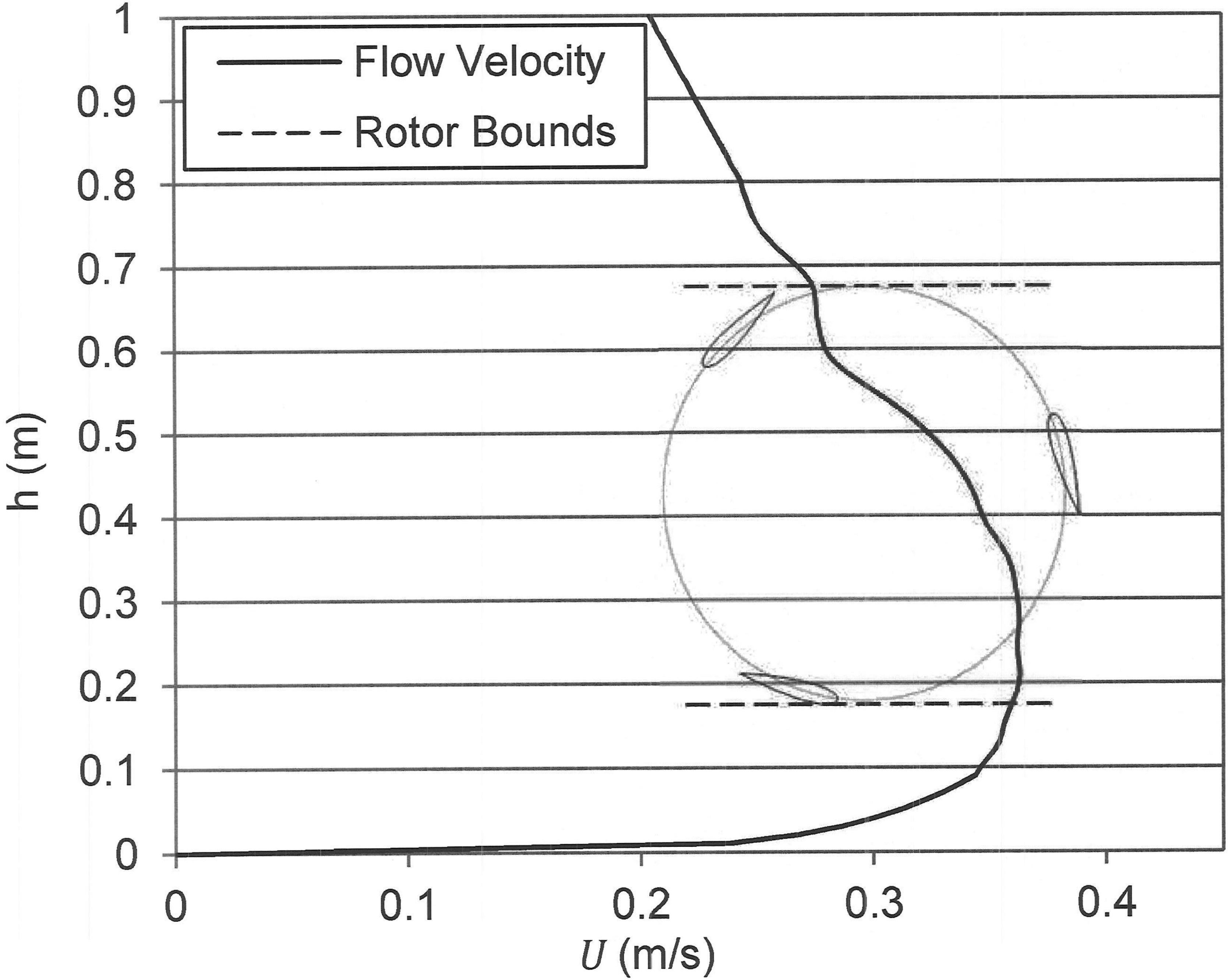
Flow Velocity
Rotor Bounds
h (m)
1
0.9
0.8
0.7
0.6
0.5
0.4
0.3
0.2
0.1
0
0.1
0.2
0.3
0.4
U (m/s)

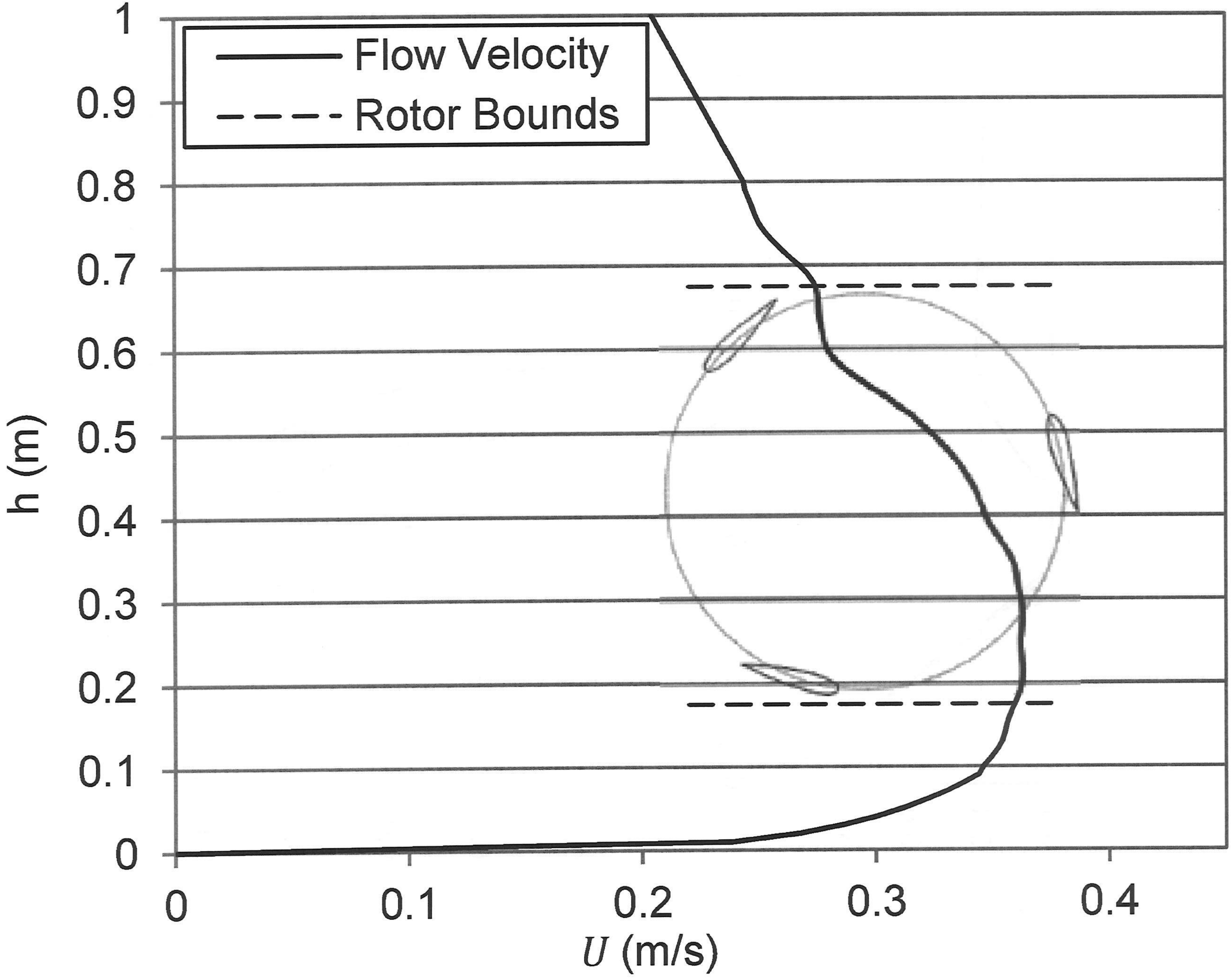
Flow Velocity
Rotor Bounds
h (m)
U (m/s)
0
0.1
0.2
0.3
0.4
0.5
0.6
0.7
0.8
0.9
1

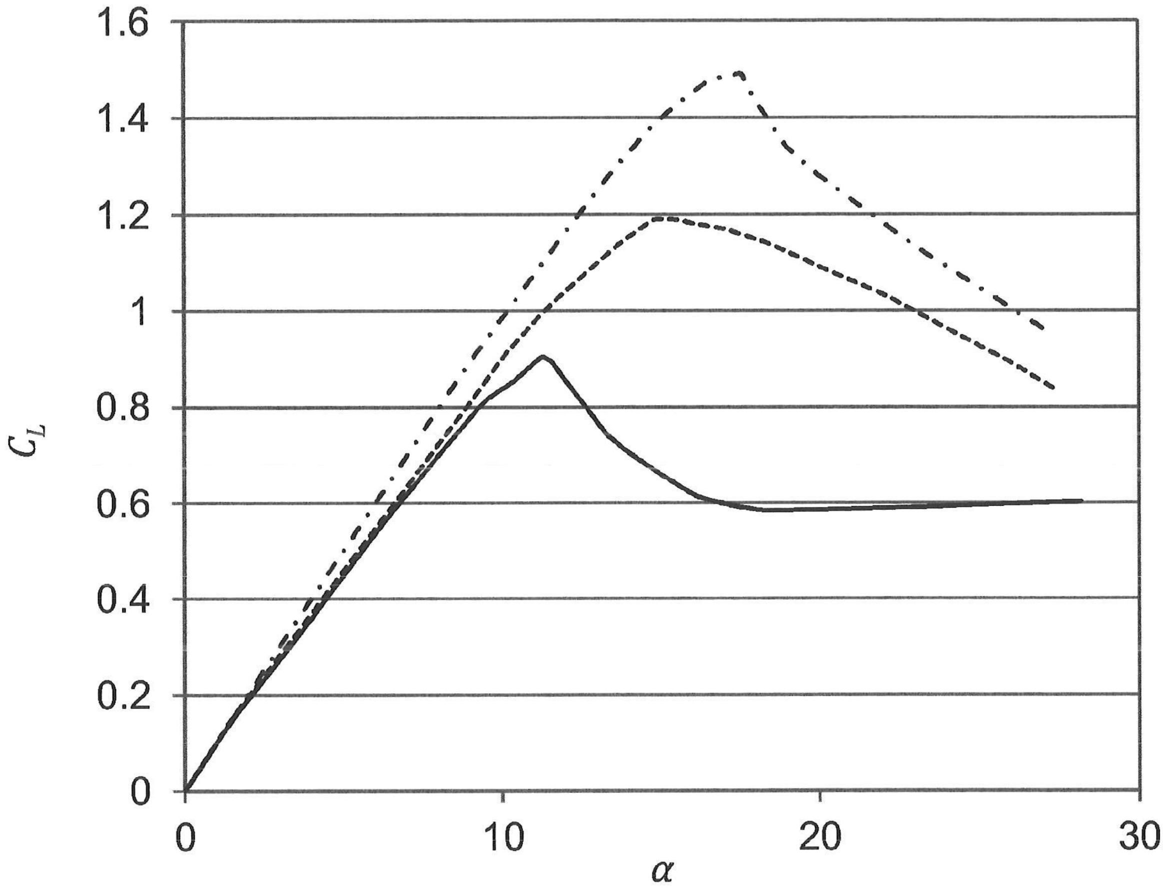
1.6
1.4
1.2
1
0.8
0.6
0.4
0.2
0
C_L
0
10
20
30
α

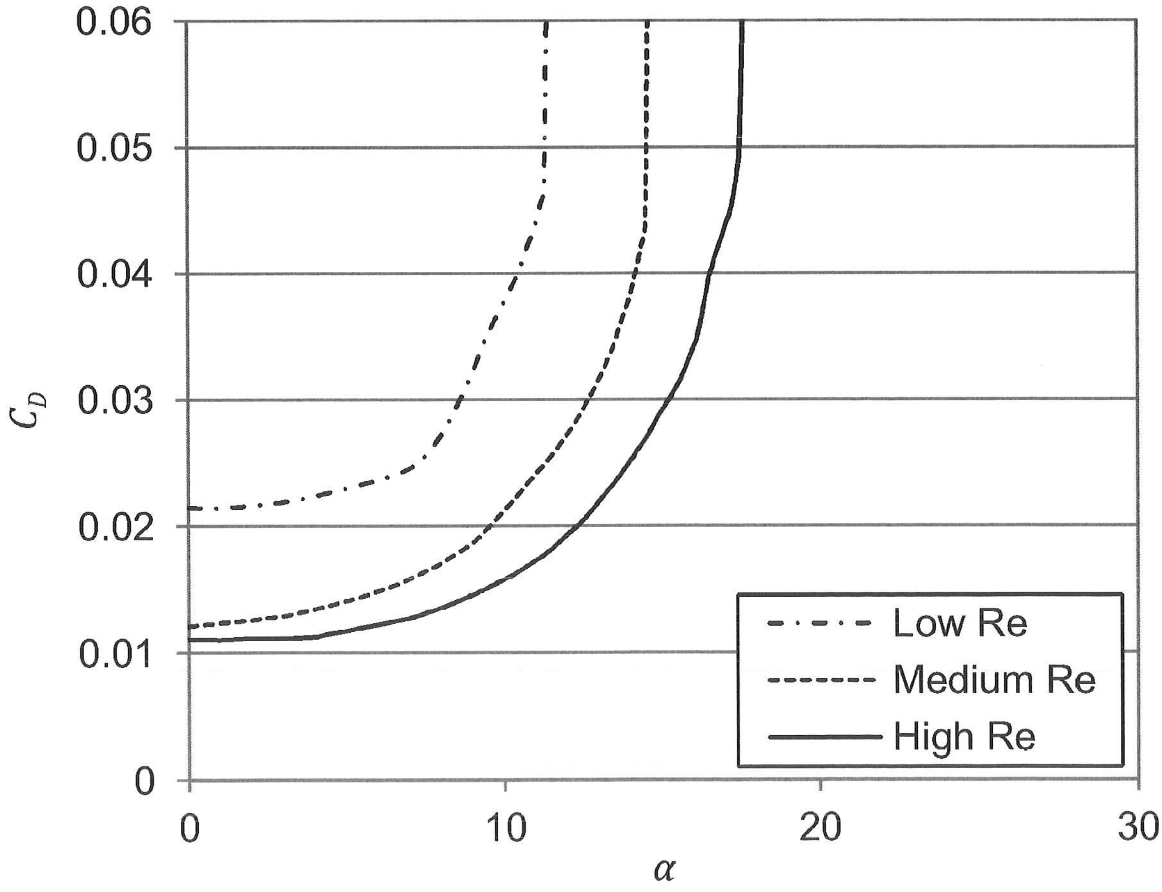
0.06
0.05
0.04
0.03
0.02
0.01
0
C_D
0
10
20
30
α
Low Re
Medium Re
High Re

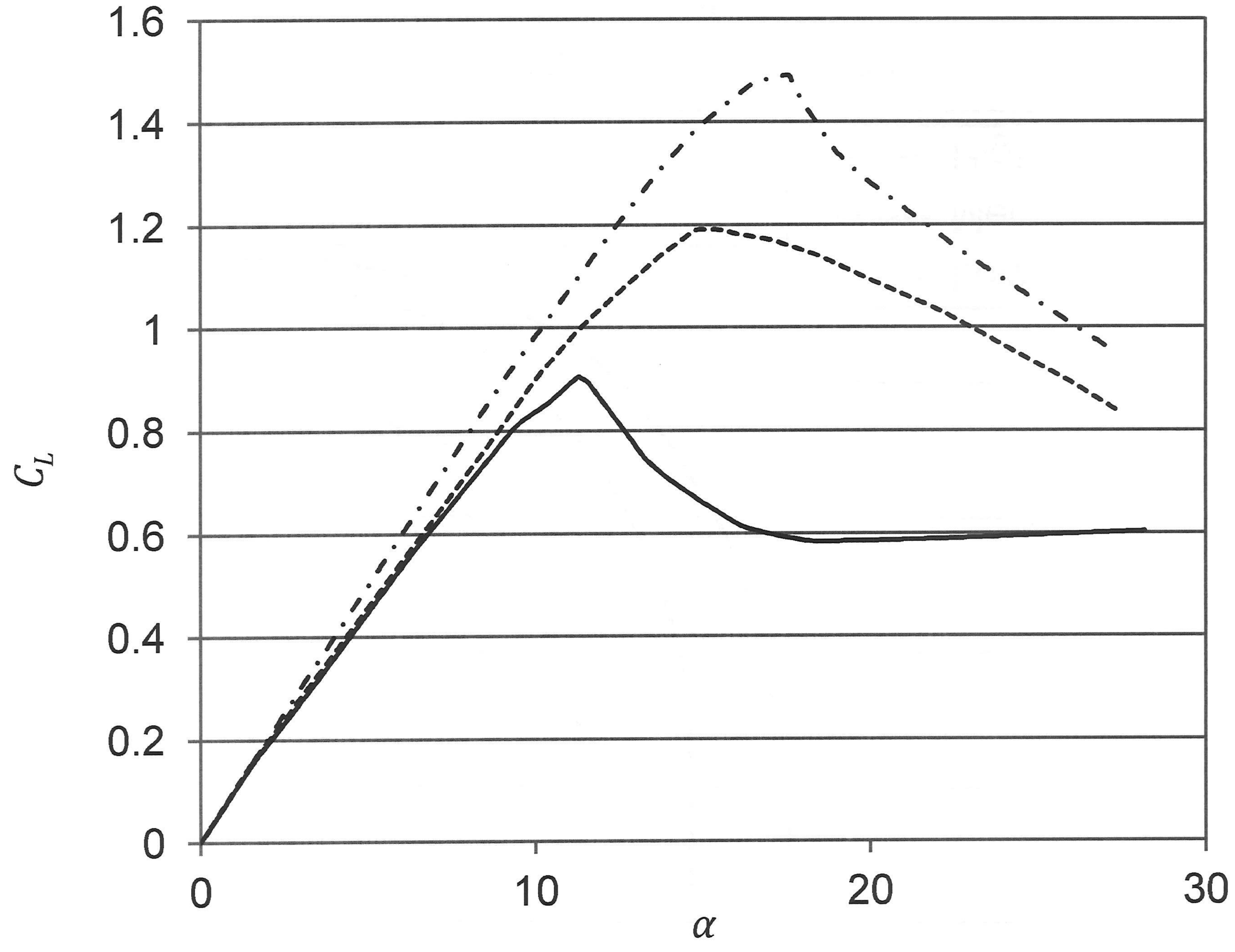
1.6
1.4
1.2
1
0.8
0.6
0.4
0.2
0
C_L
0
10
20
30
α

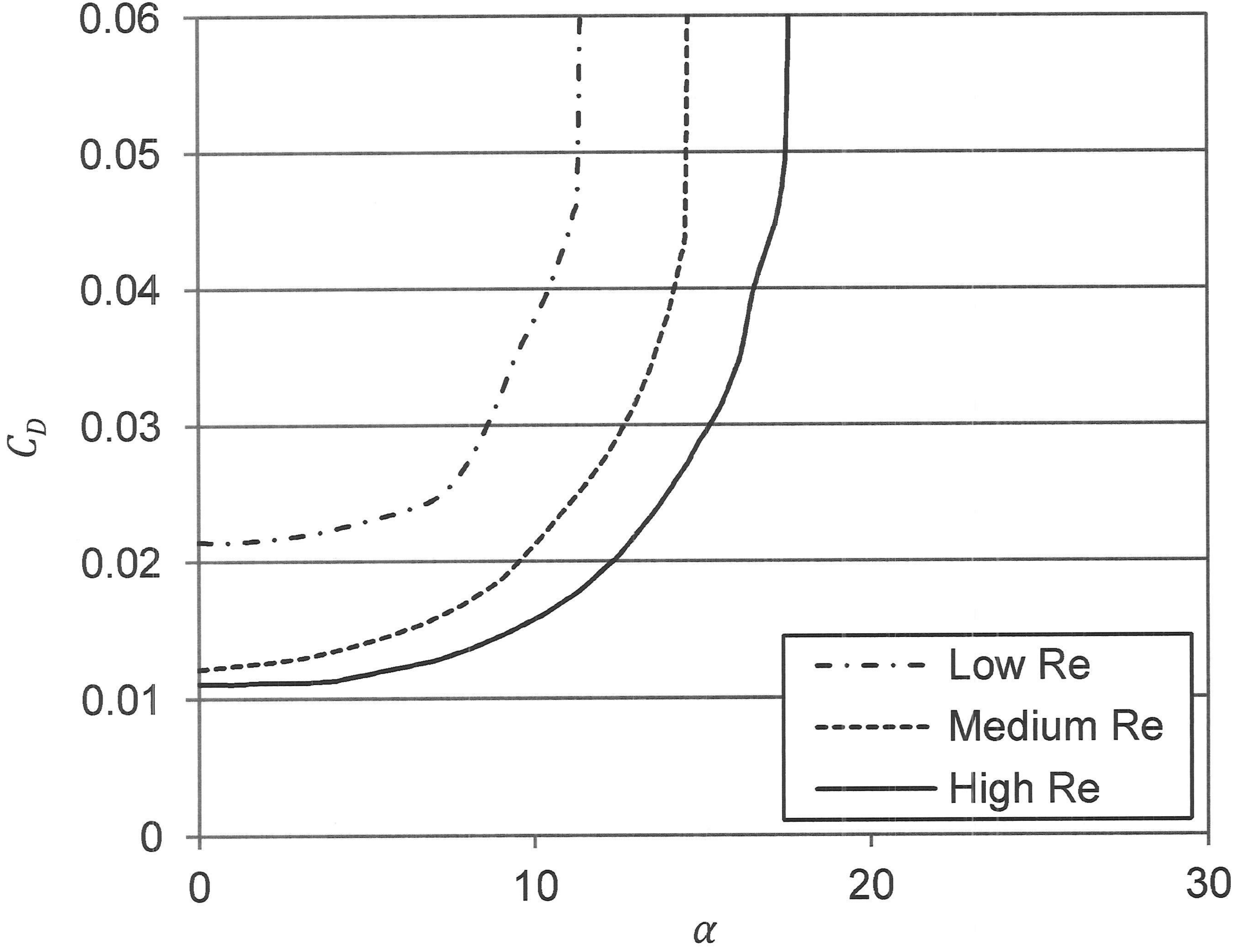
0.06
0.05
0.04
0.03
0.02
0.01
0
C_D
0
10
20
30
α
Low Re
Medium Re
High Re

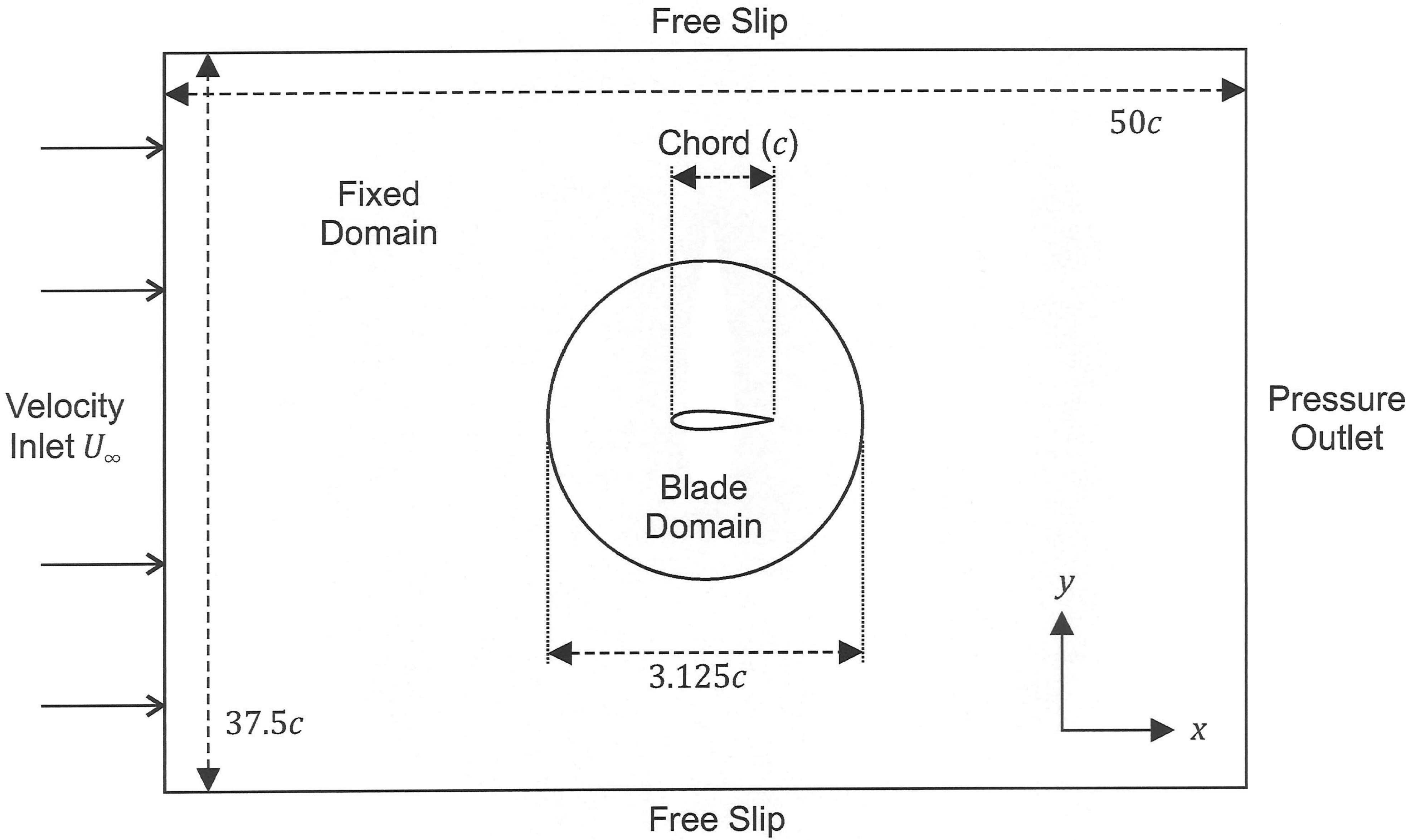
Free Slip
50c
Chord (c)
Fixed
Domain
Velocity
Inlet U_∞
Blade
Domain
Pressure
Outlet
3.125c
37.5c
y
x
Free Slip

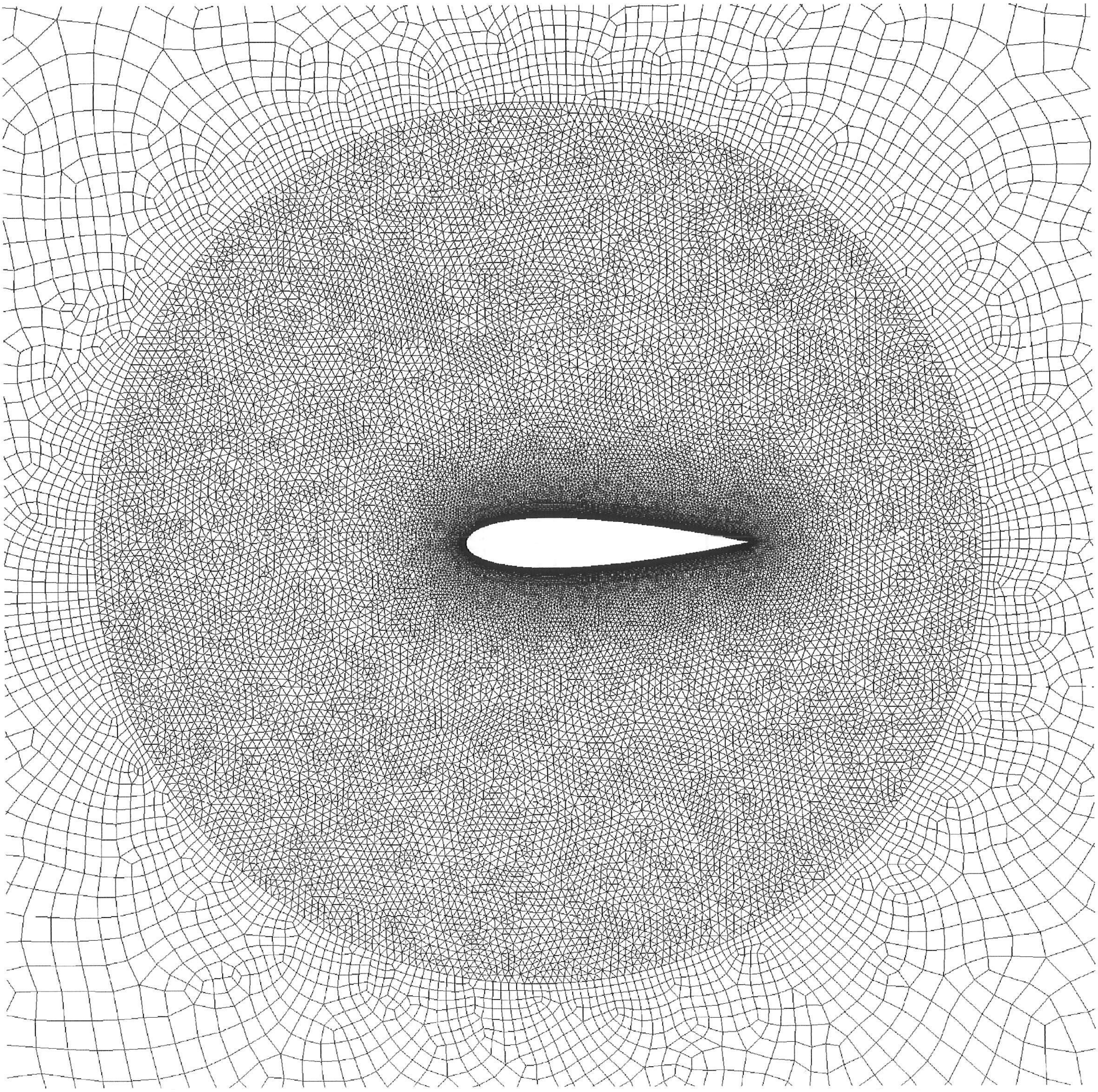

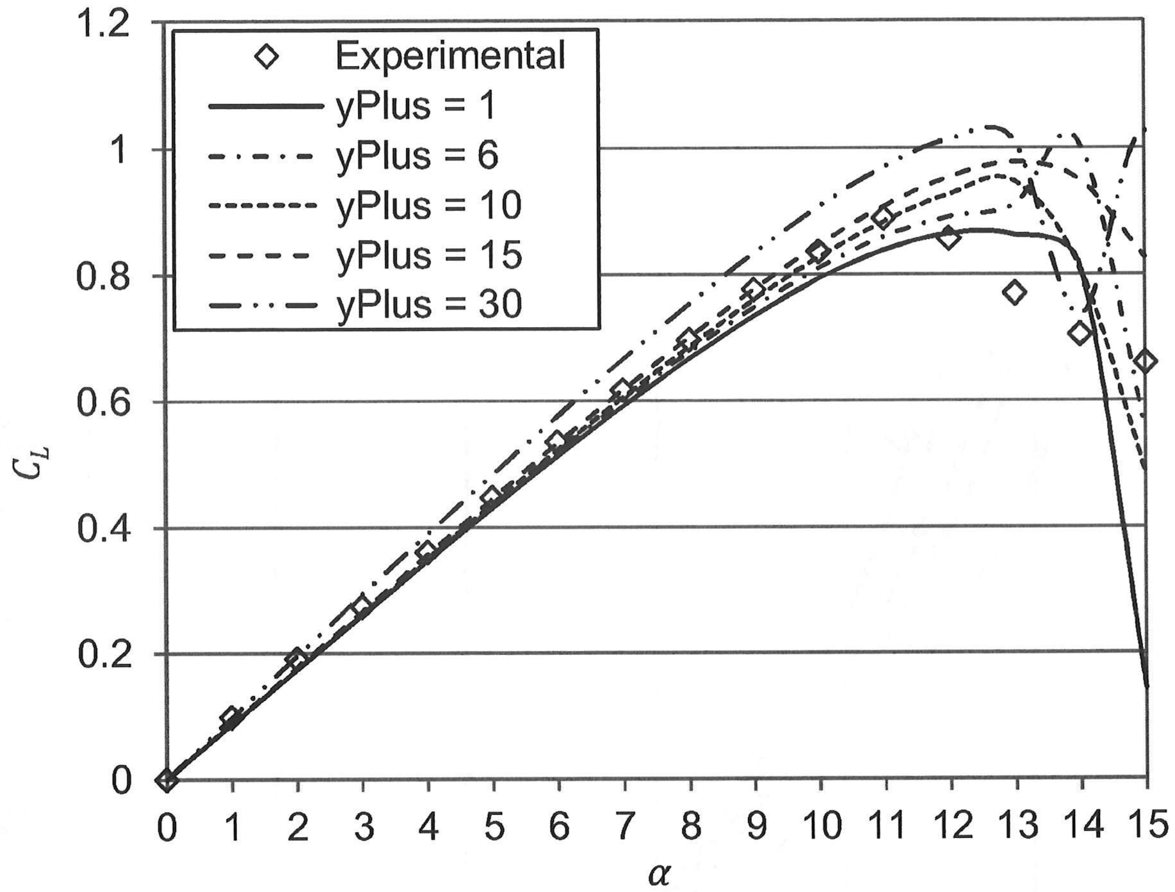

Experimental
yPlus = 1
yPlus = 6
yPlus = 10
yPlus = 15
yPlus = 30
C_L
α
1.2
1
0.8
0.6
0.4
0.2
0
0 1 2 3 4 5 6 7 8 9 10 11 12 13 14 15

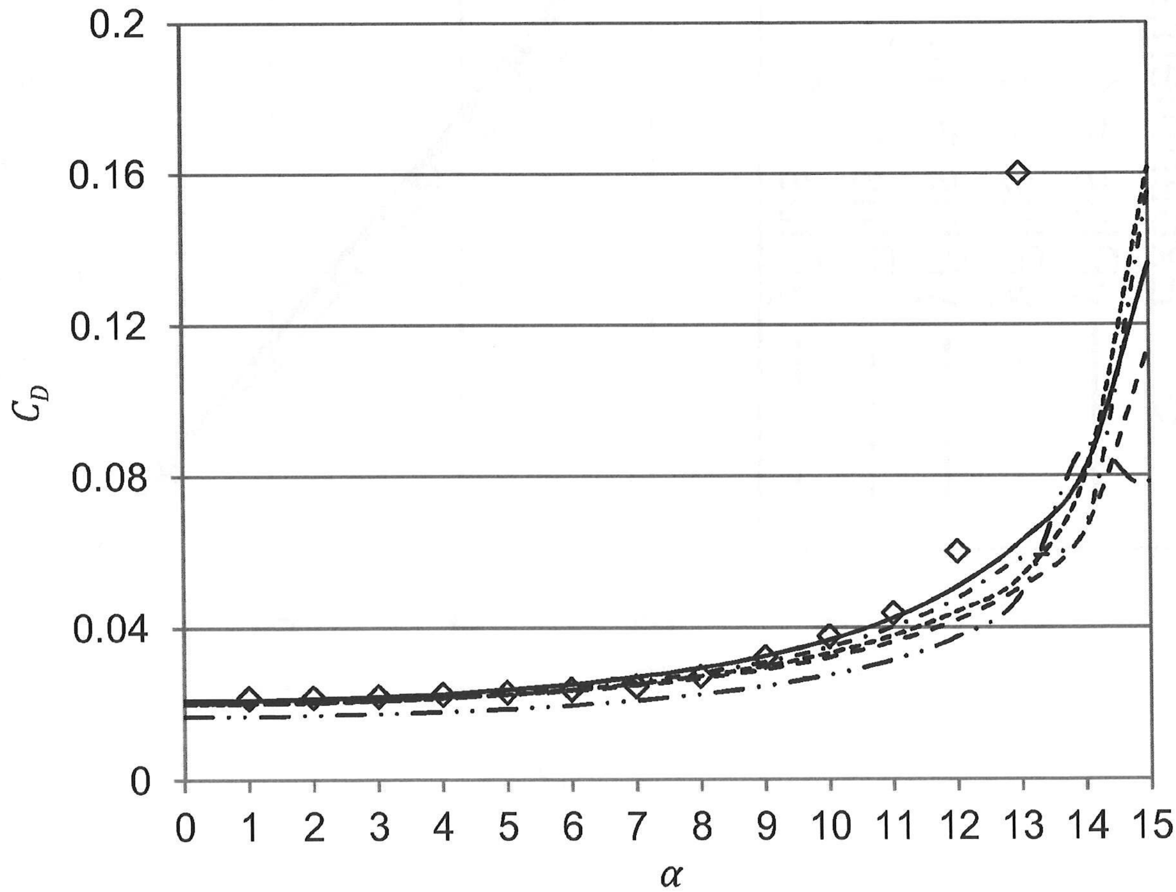

C_D
α
0.2
0.16
0.12
0.08
0.04
0
0 1 2 3 4 5 6 7 8 9 10 11 12 13 14 15

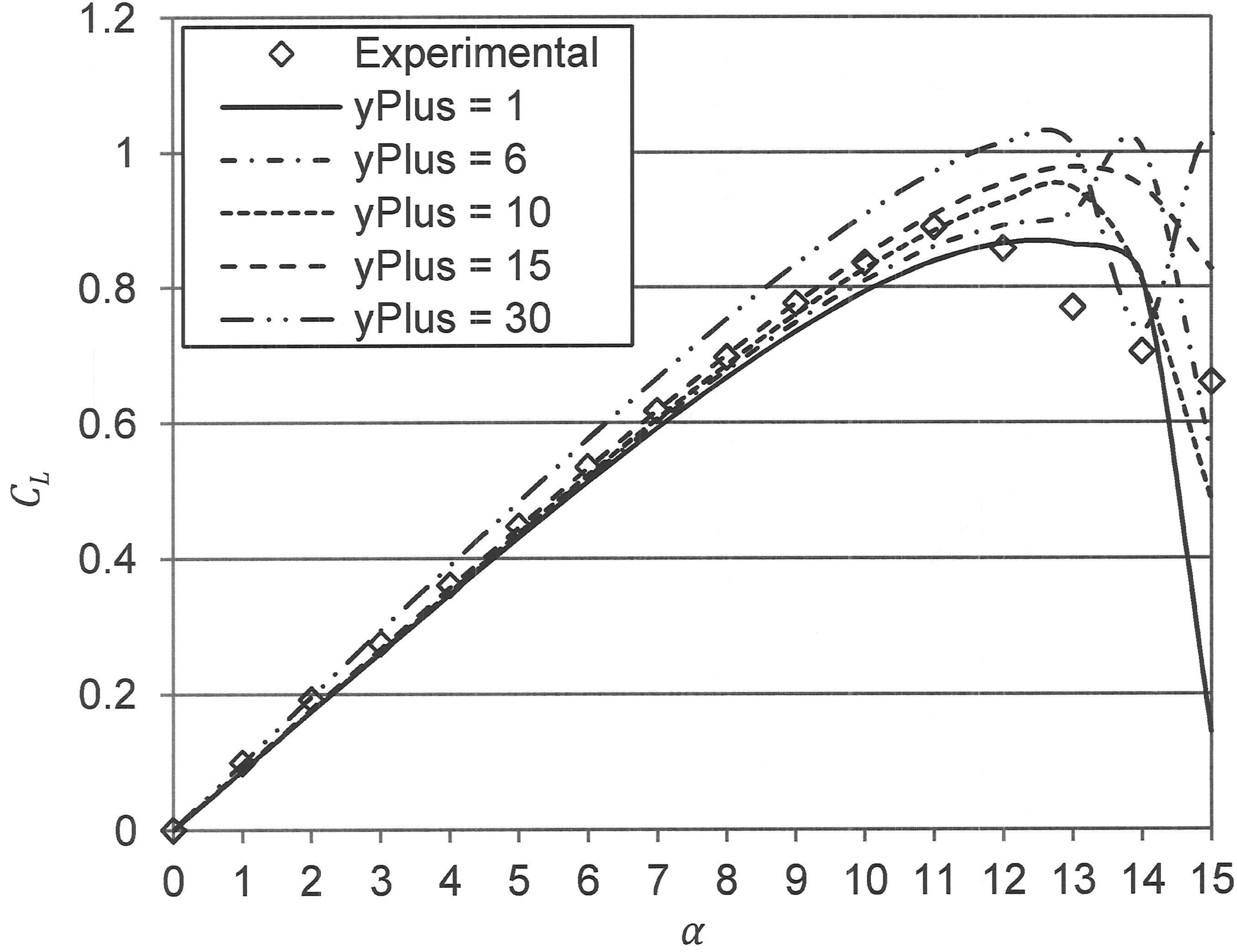

Experimental
yPlus = 1
yPlus = 6
yPlus = 10
yPlus = 15
yPlus = 30
C_L
1.2
1
0.8
0.6
0.4
0.2
0
0
1
2
3
4
5
6
7
8
9
10
11
12
13
14
15
α

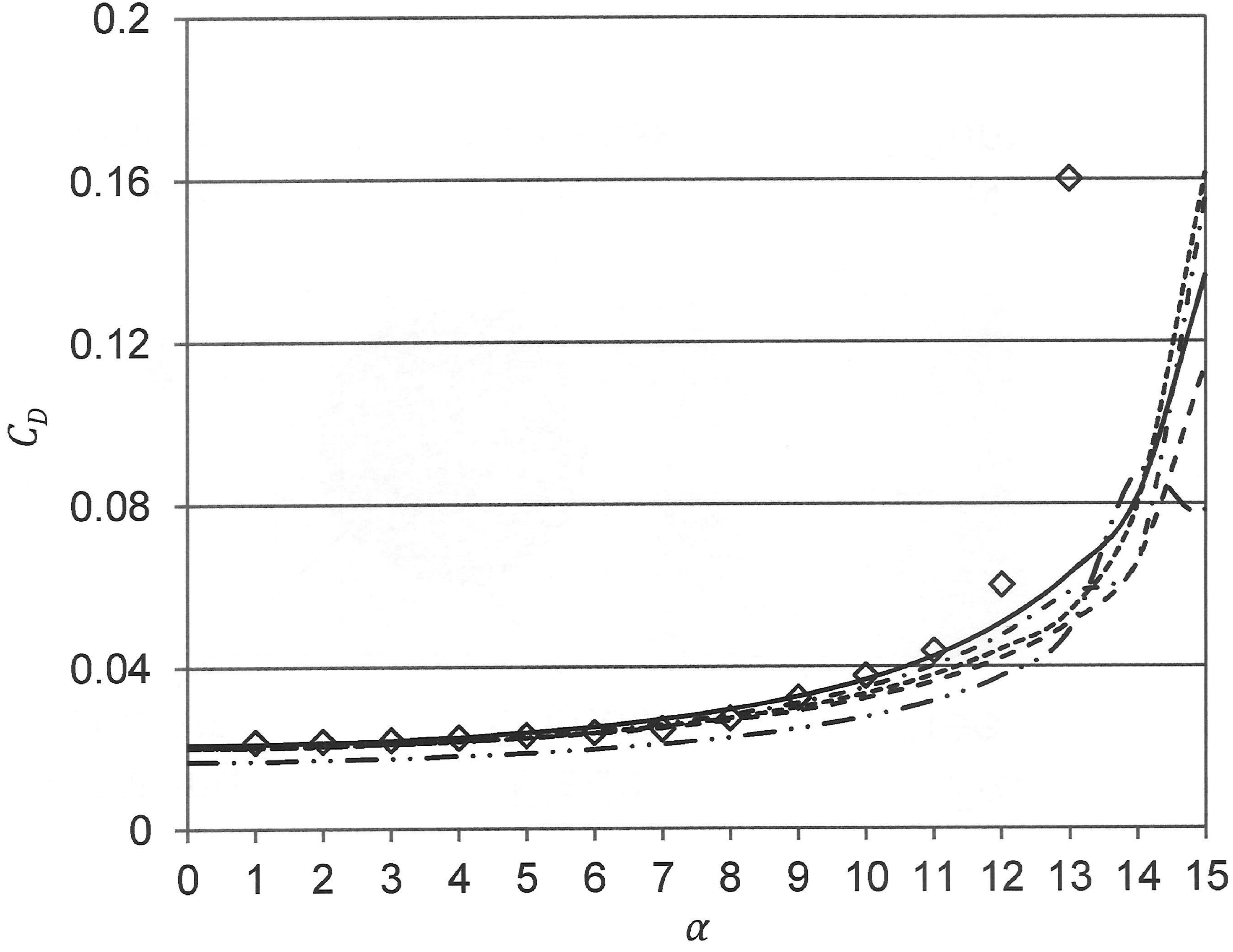

0.2
0.16
0.12
0.08
0.04
0
C_D
0 1 2 3 4 5 6 7 8 9 10 11 12 13 14 15
α

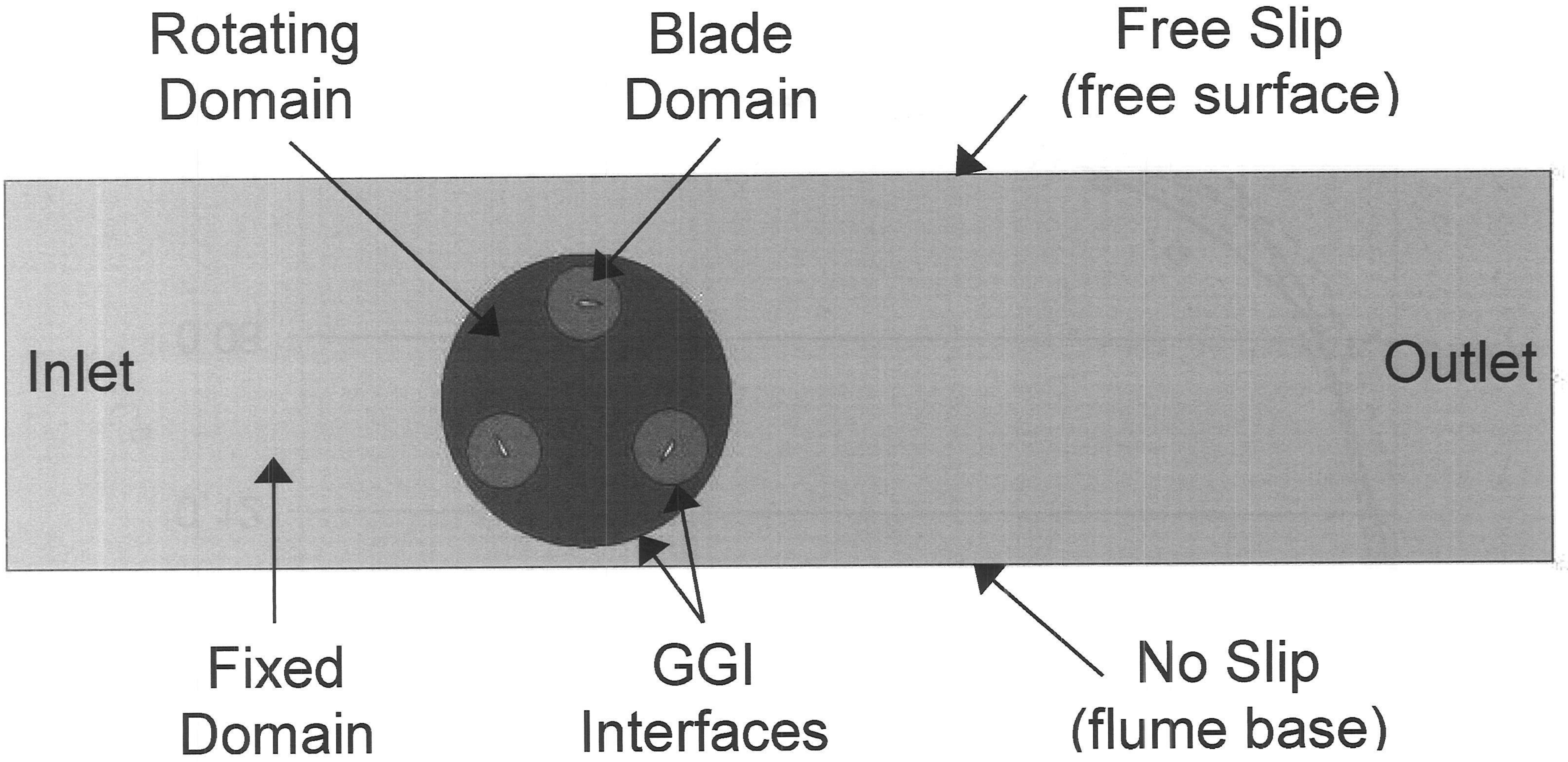
Rotating
Domain
Blade
Domain
Free Slip
(free surface)
Inlet
Outlet
Fixed
Domain
GGI
Interfaces
No Slip
(flume base)

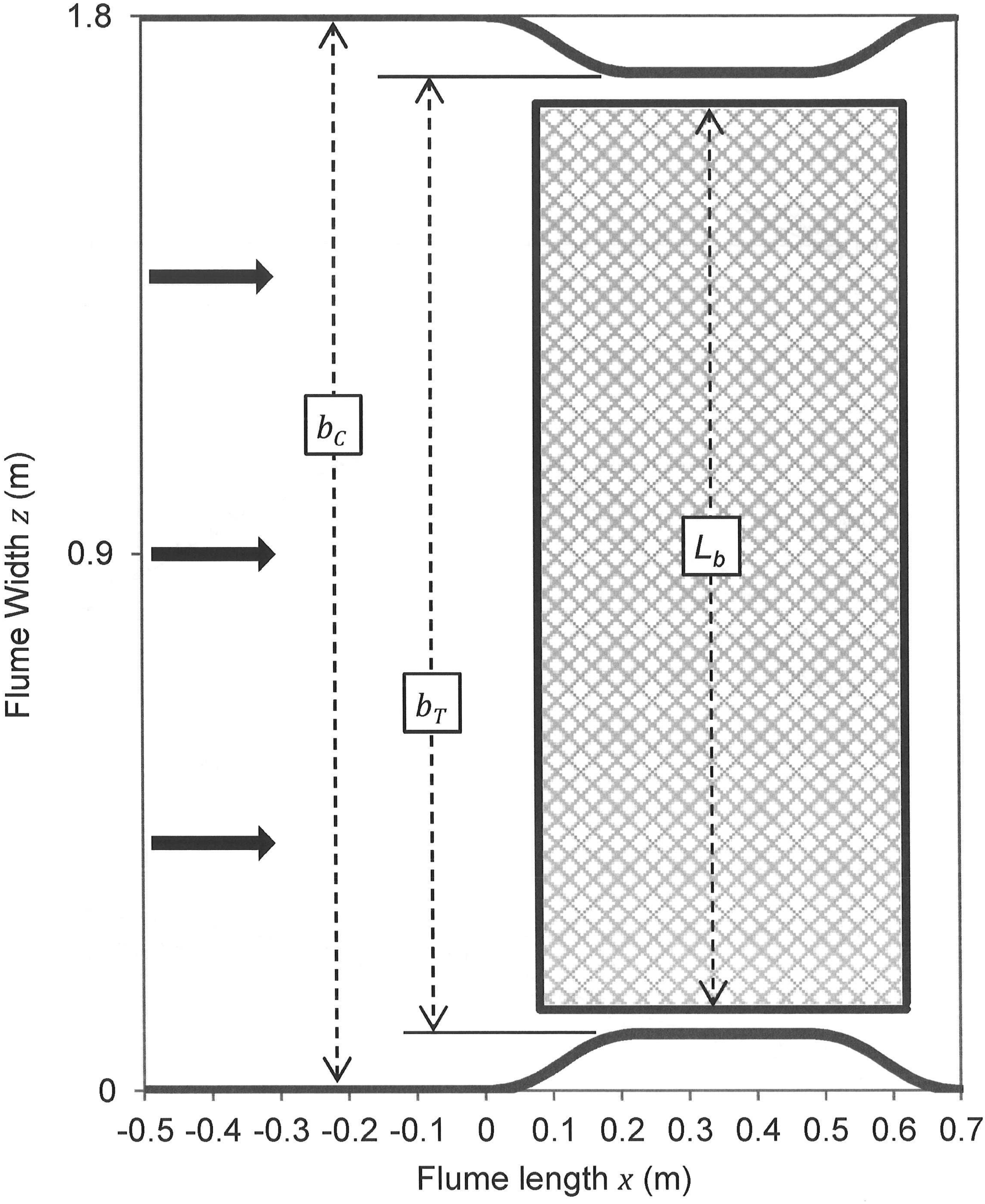

1.8
0.9
0
Flume Width z (m)
b_C
b_T
L_b
-0.5 -0.4 -0.3 -0.2 -0.1 0 0.1 0.2 0.3 0.4 0.5 0.6 0.7
Flume length x (m)

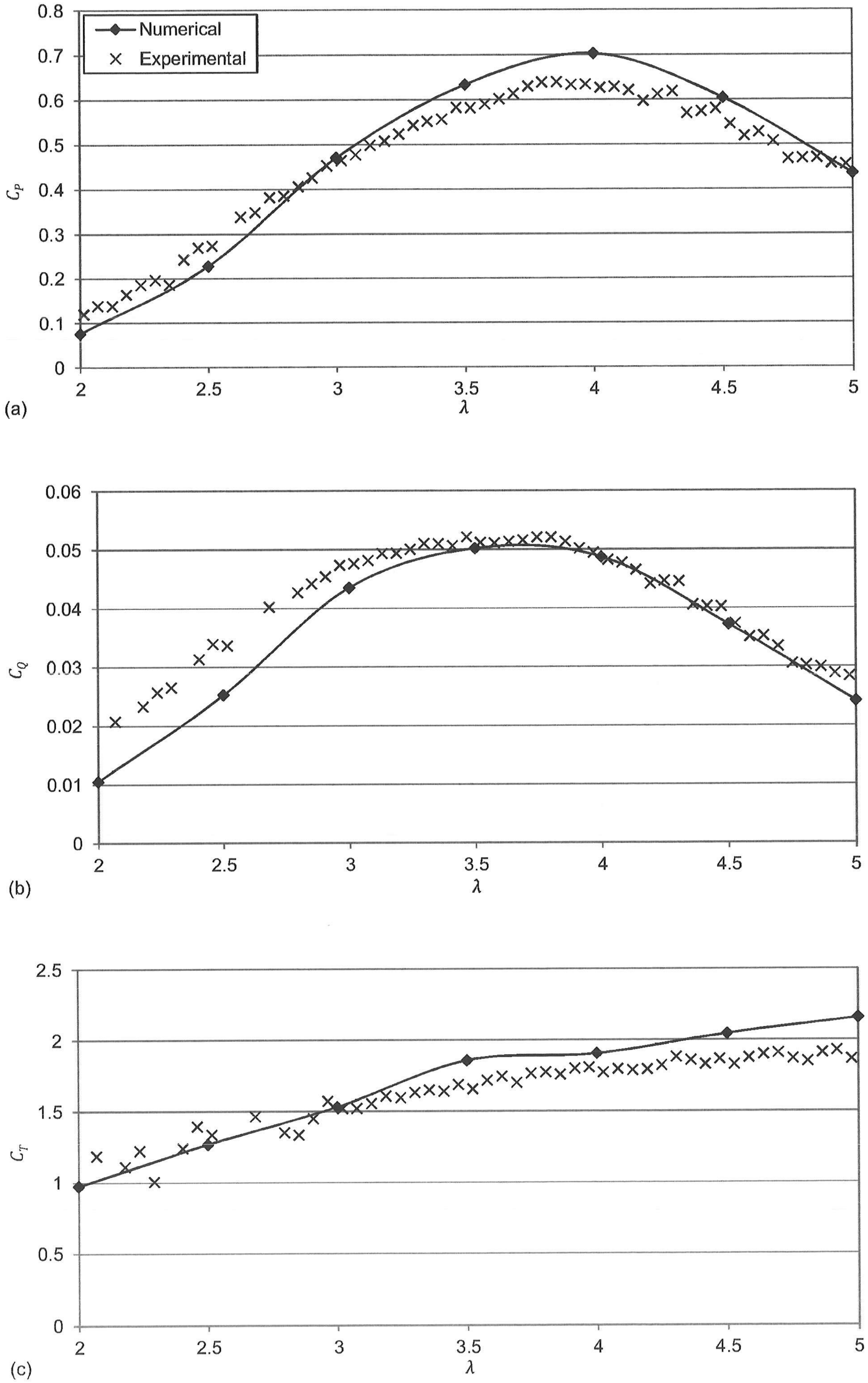

Numerical
Experimental
C_P
0.8
0.7
0.6
0.5
0.4
0.3
0.2
0.1
0
2
2.5
3
3.5
4
4.5
5
λ
(a)
C_Q
0.06
0.05
0.04
0.03
0.02
0.01
0
2
2.5
3
3.5
4
4.5
5
λ
(b)
C_T
2.5
2
1.5
1
0.5
0
2
2.5
3
3.5
4
4.5
5
λ
(c)

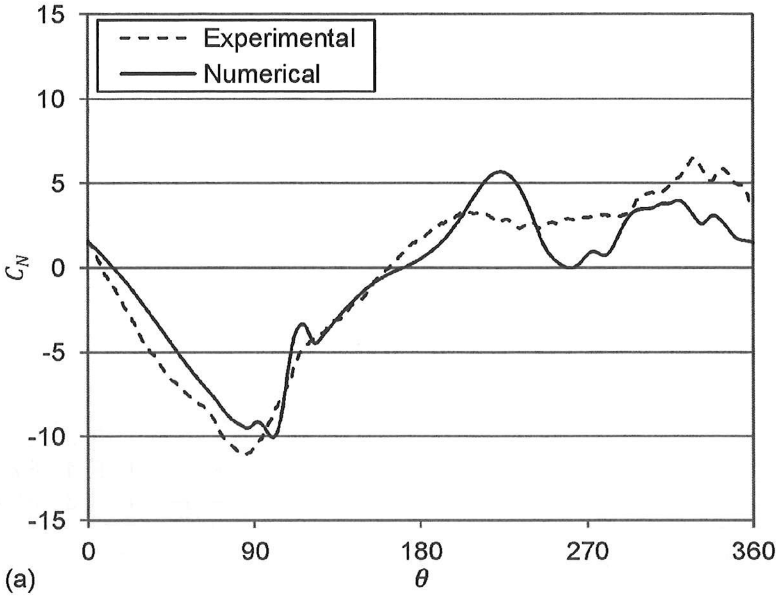
Experimental
Numerical
15
10
5
0
-5
-10
-15
C_N
0
90
180
270
360
θ
(a)

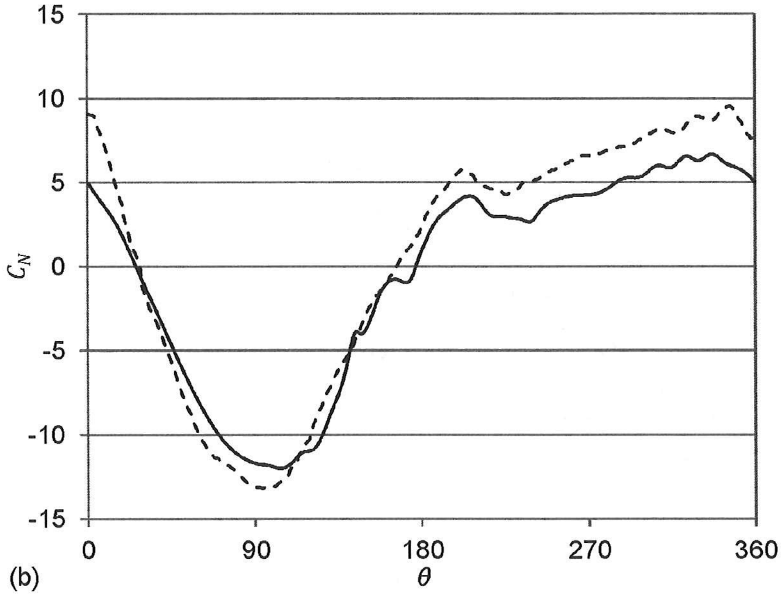
15
10
5
0
-5
-10
-15
C_N
0
90
180
270
360
θ
(b)

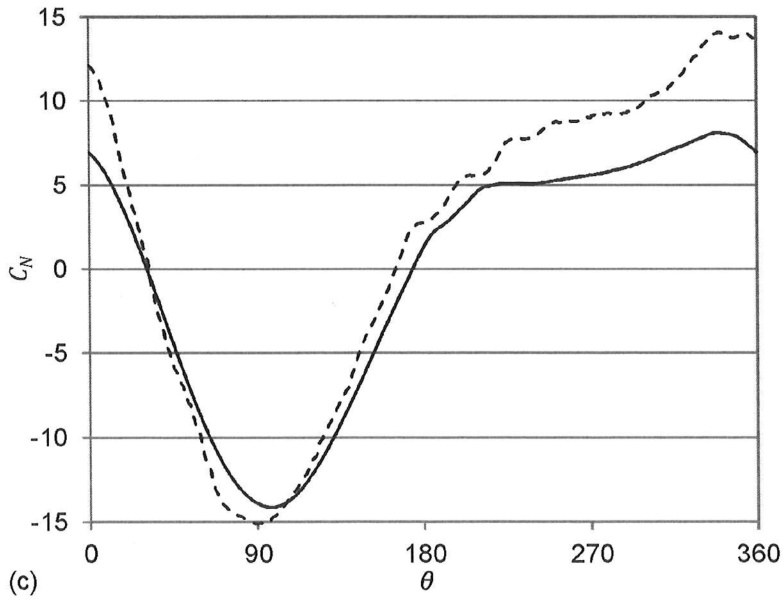
15
10
5
0
-5
-10
-15
C_N
0
90
180
270
360
θ
(c)

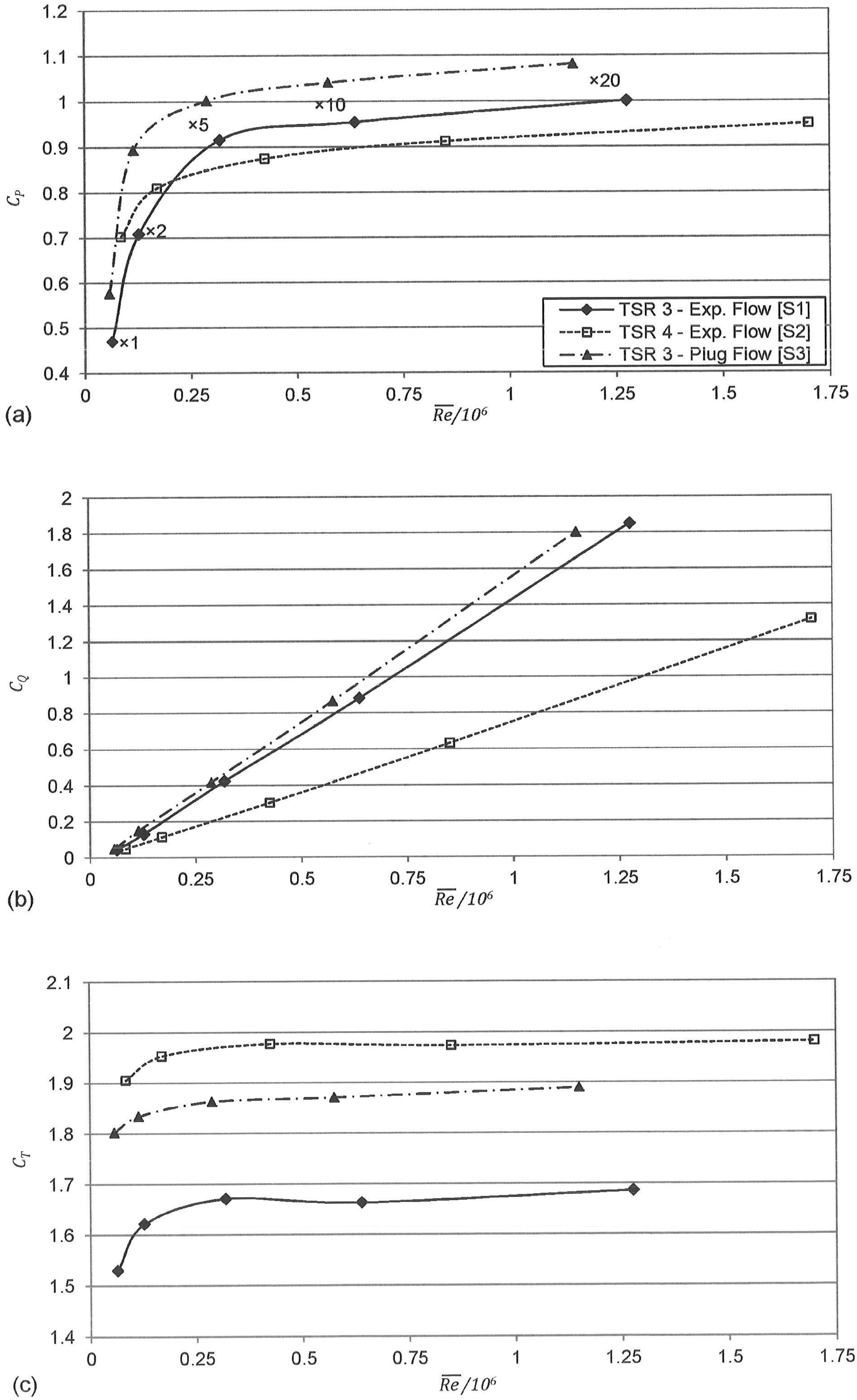

1.2
1.1
1
0.9
0.8
0.7
0.6
0.5
0.4
C_P
×1
×2
×5
×10
×20
TSR 3 - Exp. Flow [S1]
TSR 4 - Exp. Flow [S2]
TSR 3 - Plug Flow [S3]
0
0.25
0.5
0.75
1
1.25
1.5
1.75
(a)
$\overline{Re}/10^6$
2
1.8
1.6
1.4
1.2
1
0.8
0.6
0.4
0.2
0
C_Q
0
0.25
0.5
0.75
1
1.25
1.5
1.75
(b)
$\overline{Re}/10^6$
2.1
2
1.9
1.8
1.7
1.6
1.5
1.4
C_T
0
0.25
0.5
0.75
1
1.25
1.5
1.75
(c)
$\overline{Re}/10^6$

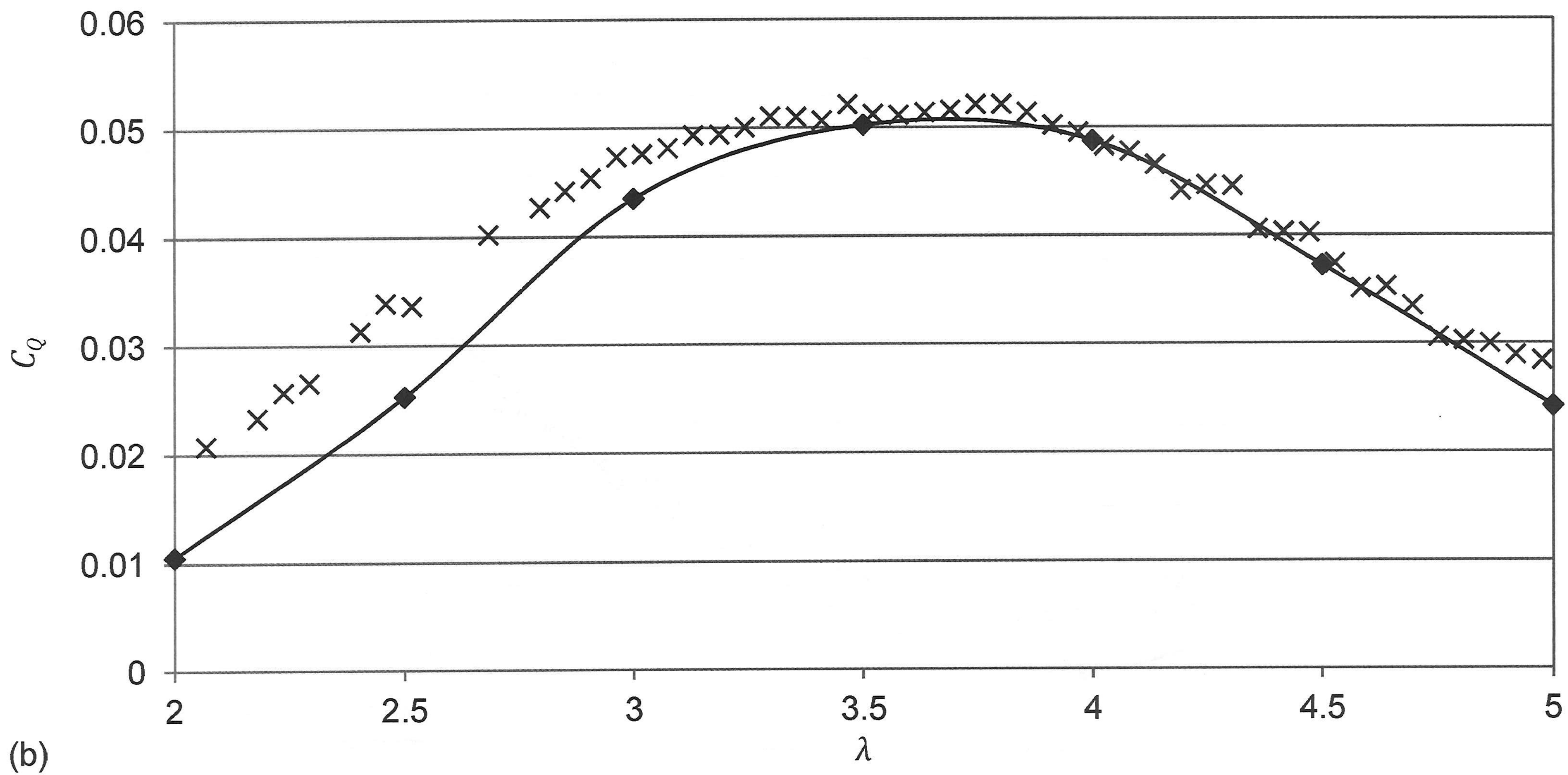

(b)

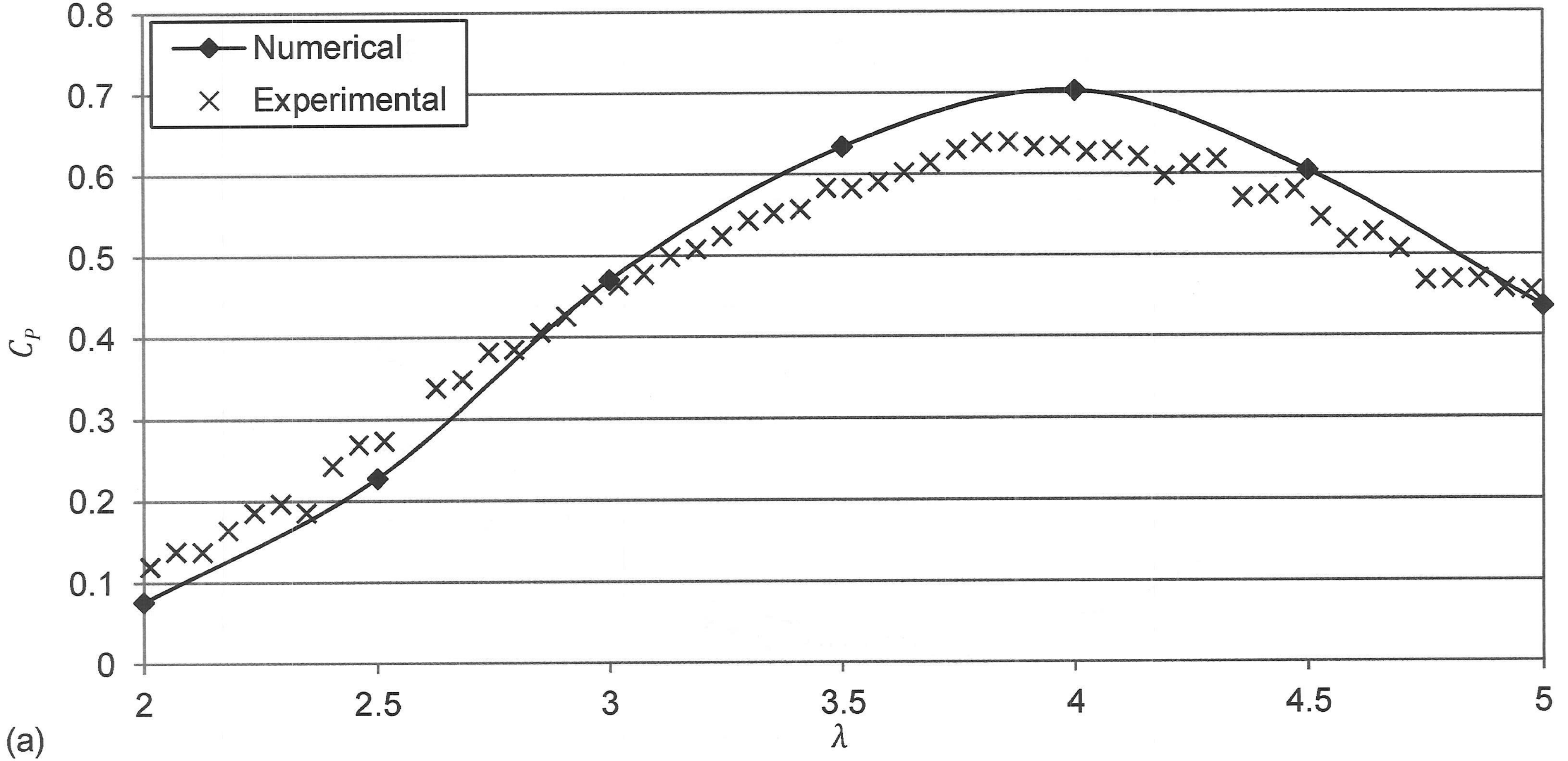
Numerical
Experimental
0.8
0.7
0.6
0.5
0.4
0.3
0.2
0.1
0
C_p
2
2.5
3
3.5
4
4.5
5
λ

(a)

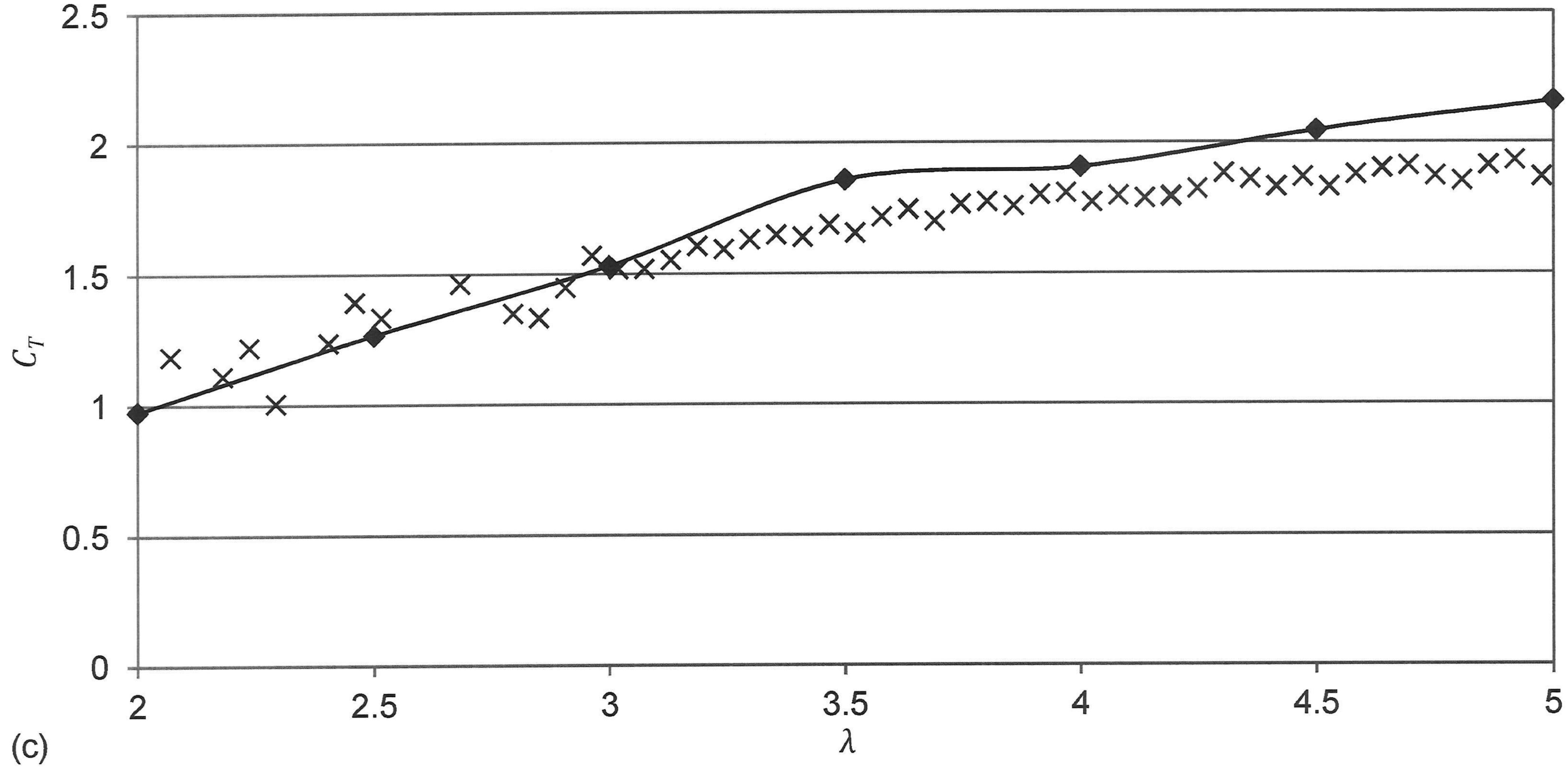

(c)